Geometric Acceleration of Complex Chemical Equilibrium Calculations – Algorithm and Application to Two- and Three-component Systems

Willem A. Roos[a,*], Johannes H. Zietsman[a,b]

[a] *University of Pretoria, Pretoria, South Africa*
[b] *Ex Mente Technologies, Pretoria, South Africa*

Abstract

A new accelerator algorithm was developed based on phase diagram geometry to include large number of equilibrium calculations into process and multiphysics models more efficiently. These models require thermochemical properties from equilibrium calculations such as phase compositions and phase fractions, heat capacity and enthalpy. When an equilibrium calculation is performed, the calculated thermochemical properties are stored in a geometrical database on the boundaries of the phase region at the calculated phase compositions. The developed accelerator can function with any commercial or open source equilibrium calculation software. In this work, ChemAppPy was used.

The lever rule can be used to interpolate thermochemical properties at any system composition within a phase region based on thermochemical properties stored on the phase region's boundaries. It is therefore only necessary to discretise boundaries and not entire phase regions, except for single-phase regions. A generic form of the lever rule is presented that can be used in any phase region and in systems with any number of system components. The Gibbs phase rule is used to calculate the dimensionality of phase region boundaries and to determine the minimum number of equilibrium calculations needed to discretise these boundaries. This framework of established thermochemical theory provides a sound basis for the discretisation and interpolation routines of the algorithm and allows the accelerator to be used with systems with any number of components. The functionality of the accelerator algorithm was tested in a number of two- and three-component systems as these systems could still be easily visualised to verify the functioning of the newly developed algorithm.

Keywords: equilibrium calculations; CALPHAD; acceleration; generic lever rule; Gibbs phase rule; process and multiphysics models

1. Introduction

Incorporating multicomponent, multiphase, high-temperature, complex chemical equilibrium calculations, hereafter simply referred to as equilibrium calculations, into multiphysics and process models, hereafter simply referred to as models, can provide valuable insight. The word "model" in this work is not associated with thermochemical solution models. Equilibrium calculations provide phase fractions, phase compositions, physical properties such as heat capacity and thermochemical properties such as enthalpy as functions of system temperature, pressure, and composition. Some additional material properties that may be required by models are not provided by equilibrium calculations. However, material property models can estimate additional properties such as viscosity, density, thermal and electrical conductivity based on equilibrium calculation results. Although this approach can provide more accurate material properties to models, equilibrium calculations are computationally expensive and are usually omitted or incorporated in a simplified manner. The authors previously reported on mathematical and numerical aspects of equilibrium calculations and their computational expense [1].

As shown in Figure 1, there is a high-order non-linear relationship between a system's number of components and equilibrium calculation time. Multiphysics models can have thousands or even millions of mesh cells and an equilibrium calculation may need to be performed in each cell for every iteration. Figure 2a shows how single iteration calculation time increases linearly as more mesh cells are used in a multiphysics model. Multiple iterations are, however, required for convergence and multiple time steps when a transient model is solved. This can also lead to total calculation times ranging from days to years, as shown in Figure 2b. In cases with many system components, mesh cells, iterations, and time steps, direct calculations of equilibrium calculations (direct calculations) can result in infeasible solving times.

The same high-order non-linear relationship between a system's number of components and equilibrium calculation time is seen in process models. The difference is that these models do not have mesh cells to consider, but still need to perform many equilibrium calculations

when the process is divided into multiple equilibrium reactors [2]. Many calculations can be required to ensure convergence to steady state, and even more so for process simulations of transient models and when these models are used with optimisation routines. Solving times can easily become infeasible.

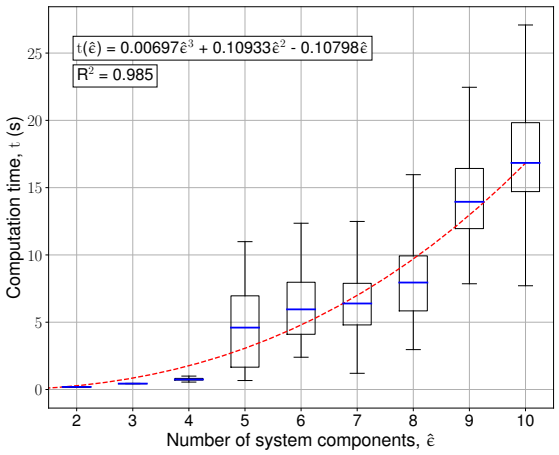

Figure 1: Third-order increase in equilibrium calculation time with number of system components. Initial system was Fe-O, and Si, Al, Mg, Ca, N, Mn, Na, K were added. 250 randomly distributed equilibrium calculations per ê-component system. Calculated with ChemAppPy [3], and data from the FToxid database in FactSage 7.2.0. The calculations were done in serial on an Intel Core i7-3770 (4 cores) with a clock speed of 3.4 GHz and had 8 GB of RAM available.

Several methods have been developed to improve the computational efficiency of including equilibrium calculations into models so that more comprehensive simulations can be done in a reasonable time. This includes methods such as creating look-up tables prior to the simulation or during (in-situ), fitting piecewise polynomial functions to thermochemical properties, phase diagram discretisation, sensitivity derivatives, artificial neural networks, and parallelisation. These methods either improve the efficiency of equilibrium calculations or store calculation results for later recall and interpolation, which is less costly than direct calculations. The authors previously reviewed these methods and for a more in-depth discussion of these methods the reader is referred to [1].

Conceptually, an equilibrium calculation accelerator, together with data stored in its database, acts as an intermediary between a model and equilibrium calculation software, as illustrated in Figure 3. In this work, the word "database" refers to the collection of calculated thermochemical properties and not to the thermochemical database that contains thermochemical solution models. The accelerator's database can be populated prior to solving the model, or while the model is being solved (in situ). When possible, the accelerator recalls stored

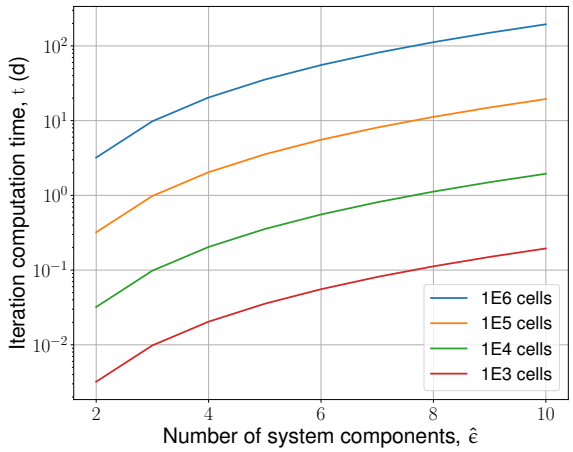

(a) Single iteration computation time of a multiphysics model, in days, as the number of mesh cells and system components increase.

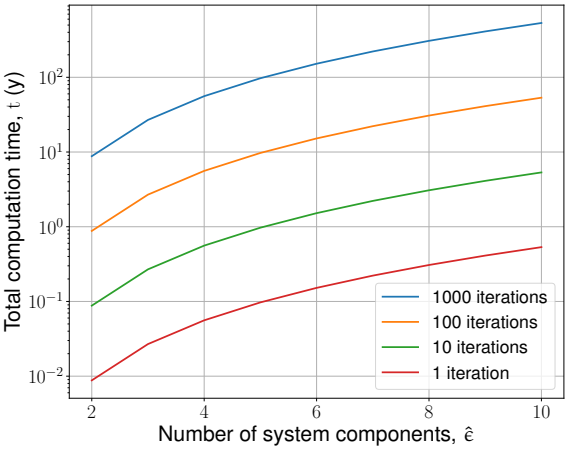

(b) Total computation time, in years, as a 1,000,000 cell multiphysics model is solved for a number of iterations.

Figure 2: Scale of the problem when equilibrium calculations are included into a multiphysics model.

data and uses it in an interpolation scheme to calculate thermochemical properties $\tilde{\mathbf{Y}}^{\sigma}$ rather than performing a more computationally expensive equilibrium calculation to obtain the thermochemical properties $\mathbf{Y}^{\sigma}$.

In this work, an accelerator algorithm was developed based on the initial work done by Zietsman [4] and lessons learnt from a review done on previous acceleration methods by Roos and Zietsman [1]. The high-level algorithm approach is discussed in Section 2 and foundational concepts required for the algorithm development explained in Section 3. Thereafter, a short demonstration in Section 4 of the foundational concepts applied to a two- and three-component system. The development of the algorithm is discussed in Section 5 and is divided into the three main routines; discretisation, storage and recall, and interpolation. Although the algorithm was developed to be generic for systems with any number of

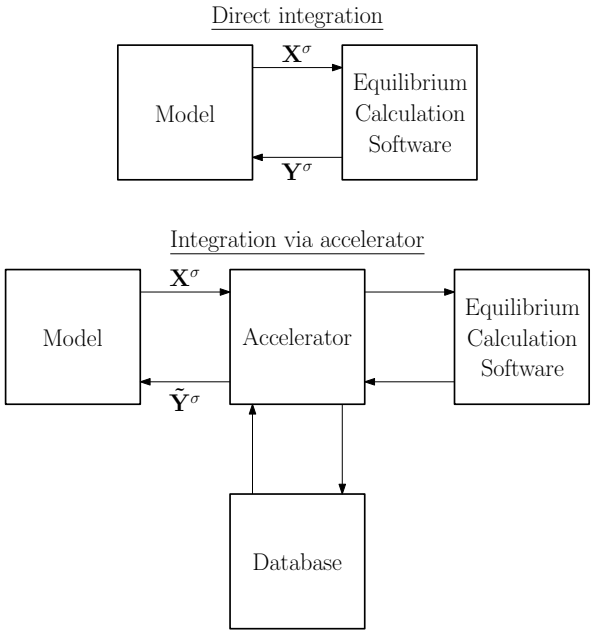

Figure 3: Schematic representation of direct calculation and integration of an accelerator between a model and equilibrium calculation software. Adapted from Zietsman [4]

components, the algorithm was only tested on a number of two- and three-component alloy and slag systems in this work as these systems could still be easily visualised to verify the functioning of the algorithm. The results are presented and discussed in Section 6. Systems with more components are being tested and the results will be reported in future work.

Because the algorithm was developed to be generic, the foundational concepts, as well as the discretisation, storage, and interpolation routines are described with generic symbolic expressions. Throughout the text, some case-specific examples are used to illustrate the symbolic expressions in the context of applicable concepts or routines. A nomenclature is appended in which all symbols that are used in the text, are described.

2. Approach

The advantages and disadvantages of existing acceleration methods were reviewed and compared by Roos and Zietsman [1]. An algorithm was conceptualised that would benefit from as many of the advantages as possible. The main conclusions from the review are presented below.

2.1. Geometrical Map of Thermochemical System

Based on the work of ten Cate et al. [5], Qiu et al. [6], Zhao et al. [7], Voskov and Tchelepi [8], and Voskov and Tchelepi [9], it was concluded that (1) a phase diagram is a geometric representation of a thermochemical system, (2) phase regions and boundaries are represented by geometric features, and (3) linear interpolation in the phase diagram is less computationally expensive than Gibbs free energy minimisation. Equilibrium calculations can be performed and the phase compositions and thermochemical properties stored, geometrically mapping the thermochemical system to the phase diagram. Phase compositions are the primary information needed to be stored as they represent the locations on the phase region boundaries. Only the calculated thermochemical properties (or additional properties estimated from other material models) that are required by the model have to be stored at the phase compositions and any unnecessary properties can be discarded. Once the system, or parts thereof, are represented by geometric features, can interpolation and the lever rule be employed to calculate the required thermochemical properties, within reasonable accuracy, at system temperatures and compositions where equilibrium calculations have not been performed yet. It was decided to develop an algorithm that maps the thermochemical system geometrically to its phase diagram.

2.2. Phase Region Boundary Discretisation

It was noticed in the work by ten Cate et al. [5] that entire phase regions where discretised and thermochemical properties stored throughout the entire region. This is unnecessary because the Gibbs phase rule reduces dimensionality to the number of degrees of freedom. The lever rule then enables the calculation of thermochemical properties at any temperature, pressure and composition within a phase region when the phase compositions and thermochemical properties on the phase region boundaries are known. The lever rule can be used in any system regardless of the number of components and in any phase region; it does not reduce dimensionality in single-phase regions, though. Therefore, only the phase region boundaries have to be discretised, apart from single-phase regions, reducing the size of the database. The lever rule is applied in an isobaric and isothermal tie simplex whose vertices are equilibrium compositions of stable phases (see Section 3.5). By storing the tie simplices, as in [8] and [9], entire phase regions can be described based on a small number of direct calculations. It was decided to employ the Gibbs phase rule to reduce the dimensionality of geometric features that need to be calculated and stored, and tie simplices, together with the lever rule, to reduce calculation time.

2.3. In-situ Discretisation

Some methods make use of pre-calculated data, whether it is to populate a database or train a neural network. This requires detailed prior knowledge of the system because temperature and composition ranges have to be specified and the data generated within these ranges. If the ranges are set too widely, unnecessary data is generated, increasing the storage size requirement and the calculation time prior to solving the model. If the

ranges are set too narrowly, the model may require data that is not contained within the database.

In the work done by Pope and Maas [10], Liu and Pope [11], and Lu and Pope [12] an in-situ discretisation method was employed. Initially the database is empty. As the model requires data, the database is queried, and if no data is available for interpolation, it is generated by performing an equilibrium calculation and storing the results for future queries. In doing this, data is generated in parts of the system that the model accesses regularly and reduces the amount of unnecessary data present in the database. Another advantage of reducing database size is that searching time for usable datasets is reduced as well. Minimal prior data of the system is required seeing that the accelerator creates its own database while the model is being solved. For these reasons, it was decided to populate the database in-situ.

3. Foundational Concepts

Before the algorithm is discussed, the key concepts that the algorithm is based on are presented.

3.1. The Gibbs Phase Rule

For a phase region with $\hat{\varphi}$ phases in a system with $\hat{\epsilon}$ independent components and $\hat{\psi}$ varying non-compositional potentials the Gibbs phase rule (Equation (1)) specifies the number of degrees of freedom f, which is the number of independent intensive variables that need to be specified, to fully define the system [13].

$$\mathrm{f} = \hat{\epsilon} - \hat{\varphi} + \hat{\psi} \tag{1}$$

As shown in Equation (2), the number of independent system components $\hat{\epsilon}$ is equal to the number of chemical elements $\hat{\varepsilon}$ minus the number of system compositional constraints $\hat{\zeta}^{\sigma}$ [14]. An example of this is the $CaO-SiO_2$ system in which there are 3 elements, but the Ca:O and Si:O molar ratios are fixed at sufficiently high oxygen potentials. This yields only 2 independent system components.

$$\hat{\epsilon} = \hat{\varepsilon} - \hat{\zeta}^{\sigma} \tag{2}$$

Because of the importance of compositional constraints to the algorithm, Equation (3) is used as the preferred form of the Gibbs phase rule in this work.

$$\mathrm{f} = \hat{\varepsilon} - \hat{\zeta}^{\sigma} - \hat{\varphi} + \hat{\psi} \tag{3}$$

Temperature and pressure are the most common non-compositional potentials, which generally means that $\hat{\psi} = 2$. When pressure is fixed the degrees of freedom are reduced by one. In this case, only temperature contributes to f, and is indicated here as f' and calculated with Equation (4). The accelerator developed in this work is aimed at isobaric systems and therefore uses this form of the Gibbs phase rule.

$$\mathrm{f}' = \hat{\varepsilon} - \hat{\zeta}^{\sigma} - \hat{\varphi} + 1 \tag{4}$$

For isothermal conditions in isobaric systems $\hat{\psi} = 0$, and the degrees of freedom are indicated as f'' and calculated with Equation (5). This form of the Gibbs phase rule is used in the accelerator when calculations are done on isotherms at constant pressure.

$$\mathrm{f}'' = \hat{\varepsilon} - \hat{\zeta}^{\sigma} - \hat{\varphi} \tag{5}$$

3.2. Phase Diagram Geometry

The accelerator algorithm uses phase diagrams, which are projections of Gibbs energy relationships onto temperature-composition space, as geometric maps of thermochemical systems. Phase regions, phase region boundaries, univariants, and invariant points in phase diagrams are all geometric features.

The algorithm only captures data associated with single-phase features. These include single-phase regions, and single-phase boundaries of multi-phase regions. In these features more than one phase can be stable ($a_{\varphi}^{\sigma} = 1$), but only one phase can have a non-zero amount ($n_{\varphi}^{\sigma} > 0$) and therefore a phase fraction of one ($x_{\varphi}^{\sigma} = 1$). These features are referred to as one-phase-fraction (OPF) features. OPF features provide composition vertices of phase region tie simplices that are used to calculate phase fractions with the lever rule.

3.2.1. Single-phase Regions

As per the definition of an OPF feature, an entire single-phase region is such a feature, and therefore an OPF region. Examples are shown in Figure 4.

3.2.2. Multi-phase Regions

In a two-phase region, as shown in Figures 4a and 4b, there are two OPF boundaries and in three-phase regions, as shown in Figure 4b, there are three OPF boundaries. Unlike single-phase regions, OPF boundaries are not areas in two-component systems or volumes in three-component systems, but lower-dimensional objects such as curves or surfaces that bound their phase regions.

It should be noted that not all phase region boundaries are OPF boundaries. As seen in Figure 4a, there are two bounding tie simplices, $\Delta_{T_U}^{\mathcal{R}}$ and $\Delta_{T_L}^{\mathcal{R}}$. Such boundaries are not OPF boundaries seeing that more than one phase can have a non-zero amount under these conditions.

Generically, a $\hat{\varphi}$-phase region, with $\hat{\varphi} > 1$, in a $\hat{\epsilon}$-component system has $\hat{\varphi}$ OPF boundaries. These boundaries are geometric objects such as lines, curves, surfaces, volumes, and hyper-volumes.

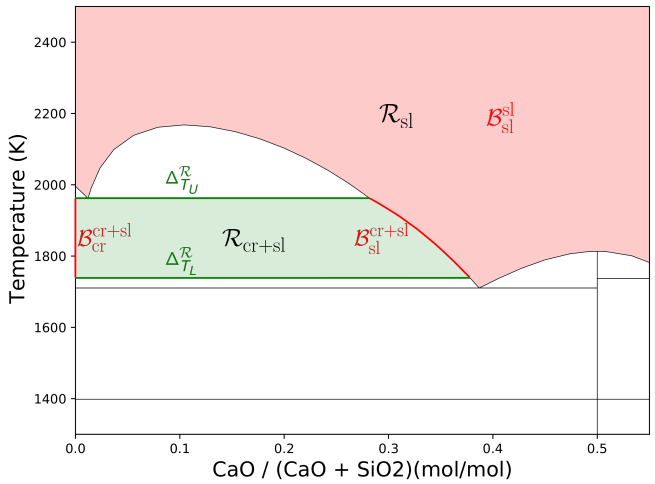

(a) The single-phase region $\mathcal{R}_{sl}$ is an OPF region $\mathcal{B}^{sl}_{sl}$, shown as the red area. The two-phase region $\mathcal{R}_{cr+sl}$, shown in green, has two OPF boundaries; the vertical red line $\mathcal{B}^{cr+sl}_{cr}$ and the red curve $\mathcal{B}^{cr+sl}_{sl}$. (sl: slag, cr: cristobalite)

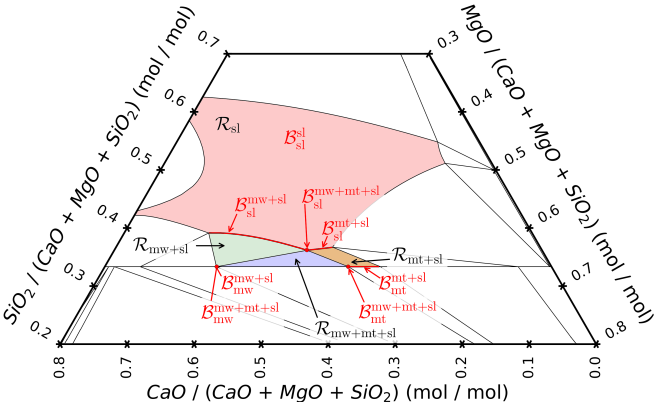

(b) The single-phase region $\mathcal{R}_{sl}$ is an OPF region $\mathcal{B}^{sl}_{sl}$, shown as the red area. The two-phase region $\mathcal{R}_{mw+sl}$, shown as the green area, has two OPF boundaries; a red curve $\mathcal{B}^{mw+sl}_{cr}$ and a red point $\mathcal{B}^{mw+sl}_{mw}$. The two-phase region $\mathcal{R}_{mt+sl}$, shown as the orange area, has two OPF boundaries; a red curve $\mathcal{B}^{mt+sl}_{sl}$ and a red line $\mathcal{B}^{mt+sl}_{mt}$. The two-phase region $\mathcal{R}_{mw+mt+sl}$, shown as the blue area, has three OPF boundaries; three red points $\mathcal{B}^{mw+mt+sl}_{mw}$, $\mathcal{B}^{mw+mt+sl}_{mt}$, and $\mathcal{B}^{mw+mt+sl}_{sl}$. (sl: slag, mw: merwinite, mt: monticellite)

Figure 4: Example OPF features in isobaric two- and three-component systems.

3.3. Dimensionality

An OPF feature's dimensional characteristics ($\mathbb{D}^{\mathcal{B}}$) determine the number of data points, and therefore the number of direct calculations, that are required for discretisation and interpolation. It is not sufficient to state that such a feature has a certain dimensionality; for example, that a phase region boundary is 1-dimensional. The system's geometric dimensionality ($\mathbb{D}^{\sigma}_{g}$), and the OPF feature's geometric ($\mathbb{D}^{\mathcal{B}}_{g}$) and functional ($\mathbb{D}^{\mathcal{B}}_{f}$) dimensionalities need to be considered.

3.3.1. System Geometric Dimensionality

The number of dimensions of the phase diagram that describes a thermochemical system is referred to as the system's geometric dimensionality $\mathbb{D}^{\sigma}_{g}$. It is calculated with Equation (6).

$$\mathbb{D}^{\sigma}_{g} = \hat{\varepsilon} - \hat{\zeta}^{\sigma} - 1 + \hat{\psi} \tag{6}$$

For the isobaric three-component system CaO–MgO–SiO$_2$ $\mathbb{D}^{\sigma}_{g} = 4 - 1 - 1 + 1 = 3$. The system is therefore described by a 3D phase diagram.

3.3.2. OPF Feature Geometric Dimensionality

OPF features can be 1D lines or curves, 2D flat or curved surfaces, 3D volumes, 4D hypervolumes, etc. For the phase j boundary of phase region i, this is referred to as its geometric dimensionality $\mathbb{D}^{\mathcal{B}^{i}_{j}}_{g}$, and it can be calculated with Equation (7).

$$\mathbb{D}^{\mathcal{B}^{i}_{j}}_{g} = \mathrm{f} \tag{7}$$

For the $\mathcal{B}^{sl}_{sl}$ region in Figure 4a $\mathbb{D}^{\mathcal{B}}_{g} = \mathrm{f} = 3-1-1+1 = 2$. This phase region is therefore a 2D surface. In the same system, the $\mathcal{B}^{cr+sl}_{cr}$ and $\mathcal{B}^{cr+sl}_{sl}$ boundaries of region $\mathcal{R}_{cr+sl}$ $\mathbb{D}^{\mathcal{B}}_{g} = 3-1-2+1 = 1$. The cristobalite boundary is therefore a line and the slag boundary a curve; both are 1D features.

Equation (7) does not describe all cases correctly for the three-component system in Figure 4b. For single-phase regions $\mathrm{f} = 4 - 1 - 1 + 1 = 3$, which correctly indicates that these regions are represented by 3D volumes. In three-phase regions $\mathrm{f} = 4-1-3+1 = 1$, which also correctly shows that the single-phase boundaries of these regions are represented by 1D lines or curves. In two-phase regions $\mathrm{f} = 4 - 1 - 2 + 1 = 2$, which states that the single-phase boundaries of such regions are 2D surfaces. This is correct when the phases consist of 2 or 3 independent components. Pure substances, however, exist as constant composition lines that only vary with temperature. A single-phase boundary can therefore not be 2-dimensional ($\mathbb{D}^{\mathcal{B}}_{g} = \mathrm{f} = 2$) if the phase only exists in 1D.

To correctly determine $\mathbb{D}^{\mathcal{B}}_{g}$, the f for the phase region must be combine with f^{φ}; the degrees of freedom when considering phase φ in isolation. f^{φ} incorporates all the phase's compositional constraints $\hat{\zeta}^{\varphi}$, and is calculated with Equation (8). $\mathbb{D}^{\mathcal{B}}_{g}$ is calculated correctly for all cases with Equation (9).

$$\mathrm{f}^{\varphi} = \hat{\varepsilon} - \hat{\zeta}^{\varphi} - 1 + \hat{\psi} \tag{8}$$

$$\mathbb{D}^{\mathcal{B}}_{g} = \min\left(\mathrm{f}, \mathrm{f}^{\varphi}\right) \tag{9}$$

3.3.3. OPF Feature Functional Dimensionality

Finally, the dimensionality of the space that an OPF feature traverses needs to be considered. This is referred to as the feature's functional dimensionality $\mathbb{D}^{\mathcal{B}}_{f}$, and it is calculated with Equation (10).

$$\mathbb{D}^{\mathcal{B}}_{f} = \mathrm{f}^{\varphi} \tag{10}$$

For a 1D OPF boundary in a 3D system that curves in all 3 dimensions $\mathbb{D}_{\mathrm{f}}^{\mathcal{B}} = 3$. When the boundary is constrained to traverse a flat plane $\mathbb{D}_{\mathrm{f}}^{\mathcal{B}} = 2$. If the phase in question is a pure substance, it is constrained to a 1D straight line and $\mathbb{D}_{\mathrm{f}}^{\mathcal{B}} = 1$.

Region $\mathcal{R}_{\mathrm{cr+sl}}$ in Figure 4a has two single-phase boundaries, $\mathcal{B}_{\mathrm{cr}}^{\mathrm{cr+sl}}$ and $\mathcal{B}_{\mathrm{sl}}^{\mathrm{cr+sl}}$, both of which are 1D features, since $\mathbb{D}_{\mathrm{g}}^{\mathcal{B}} = \mathrm{f} = 1$. Cristobalite is a pure substance, which means that $\mathcal{B}_{\mathrm{cr}}^{\mathrm{cr+sl}}$ is constrained to a single composition coordinate and it only traverses one dimension, namely temperature; therefore, for $\mathcal{B}_{\mathrm{cr}}^{\mathrm{cr+sl}}$, $\mathbb{D}_{\mathrm{f}}^{\mathcal{B}} = \mathrm{f}^{\mathrm{cr}} = 1$. In contrast, slag is a solution with two independent components (CaO and SiO_2). The $\mathcal{B}_{\mathrm{sl}}^{\mathrm{cr+sl}}$ boundary's coordinates therefore vary in both composition and temperature, which means that it traverses 2D space and $\mathbb{D}^{\mathcal{B}} = \mathrm{f}^{\mathrm{sl}} = 2$.

3.3.4. Dimensional Characteristics

The three different dimensionalities that characterise an OPF feature are related through Equation (11). All features are constrained by the geometric dimensionality of the phase diagram.

$$\mathbb{D}_{\mathrm{g}}^{\mathcal{B}} <= \mathbb{D}_{\mathrm{f}}^{\mathcal{B}} <= \mathbb{D}_{\mathrm{g}}^{\sigma} \tag{11}$$

To concisely indicate the dimensional characteristics for an OPF feature, the notation $\mathbb{D}^{\mathcal{B}} = (\mathbb{D}_{\mathrm{g}}^{\mathcal{B}} : \mathbb{D}_{\mathrm{f}}^{\mathcal{B}} : \mathbb{D}_{\mathrm{g}}^{\sigma})$ is used. For the two-component system in Figure 4a, $\mathcal{B}_{\mathrm{sl}}^{\mathrm{sl}}$ has $\mathbb{D}^{\mathcal{B}} = (2{:}2{:}2)$, $\mathcal{B}_{\mathrm{sl}}^{\mathrm{cr\text{-}sl}}$ has $\mathbb{D}^{\mathcal{B}} = (1{:}2{:}2)$, and $\mathcal{B}_{\mathrm{cr}}^{\mathrm{cr\text{-}sl}}$ has $\mathbb{D}^{\mathcal{B}} = (1{:}1{:}2)$.

3.4. Simplices

A simplex is the generalisation of a triangle in kD space, which has $\mathrm{k}+1$ vertices and is denoted by ${}_{\mathrm{k}}\Delta$. For instance, a triangle is a 2D object, referred to as a 2-simplex and denoted by ${}_{2}\Delta$. Similarly, a 3-simplex is a tetrahedron, a 1-simplex is a line, and a 0-simplex is a point. For $\mathrm{k} > 3$ simplices are beyond the authors' ability to visualise, and are simply referred to as k-simplices.

3.4.1. Content of a Simplex

The content $\nu({}_{\mathrm{k}}\Delta)$ of a k-simplex is the measure of the space contained within its vertices. Examples include the length of a line, area of a triangle, and volume of a tetrahedron. For any dimensionality k, ν is calculated with the Cayley-Menger determinant [15], which only requires the simplex's vertex coordinates.

3.4.2. Barycentric Coordinates

The barycentric coordinate system is used to express the location of a point contained within a simplex with reference to its vertices, as shown in Figure 5.

From one vertex (x_0) of the $\mathrm{k}+1$ number of vertices of a k-simplex, k number of vectors ($\mathbf{V}_{\mathrm{i}}$) are created to each of the k remaining vertices (x_{i}). A barycentric coordinate weight β_{i} is applied to each vector and the sum of weighted vectors result in the vector from the origin vertex (x_0) to the location of a point (p). The coordinates of a point inside a k-simplex can therefore be described by the $\mathrm{k}+1$ vertices of a k-simplex and a set of k barycentric coordinate weights, as shown in Equation (12).

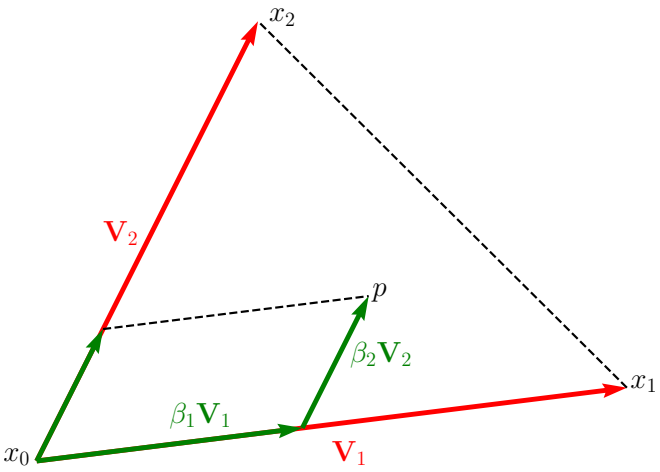

Figure 5: Barycentric coordinates describing the position of a point within a ${}_{2}\Delta$.

$$p - x_0 = \sum_{\mathrm{i}=1}^{\mathrm{k}} \beta_{\mathrm{i}} \mathbf{V}_{\mathrm{i}}$$

$$p = x_0 + \sum_{\mathrm{i}=1}^{\mathrm{k}} \beta_{\mathrm{i}} (x_{\mathrm{i}} - x_0) \tag{12}$$

The conditions of Equation (13) have to be met for a point to be contained within the k-simplex. If any of the barycentric coordinate weights are smaller than zero or larger than one, the point is outside the simplex. If the sum of weights are larger than one, the resulting vector also ends at a point outside the simplex.

$$\beta_{\mathrm{i}} \in \mathbb{R}[0,1] \quad \text{and} \quad \sum_{\mathrm{i}=1}^{\mathrm{k}} \beta_{\mathrm{i}} <= 1 \tag{13}$$

3.4.3. Discretisation by Simplices

Triangulation can be used to discretise OPF features. Lines are used for discretising 1D features, triangles for 2D features, and k-simplices for features with $\mathbb{D}_{\mathrm{g}}^{\mathcal{B}} = \mathrm{k}$. This allows an OPF feature to be discretised into elements with the same geometric dimensionality, which have the fewest number of vertices per discretisation element. This is referred to as discretisation by simplices.

3.5. Tie Simplices

For a system at equilibrium, all potentials (temperature, pressure, chemical potential, etc.) are equal in all phases present. On a phase diagram at constant pressure and temperature, phase compositions on OPF boundaries associated with multi-phase region i are connected

by a tie simplex $\Delta^{\mathcal{R}_i}$, which is an iso-chemical-potential simplex. The dimensionality k of a tie simplex is determined by the number of phases present according to Equation (14), and its number of vertices is equal to the number of phases present with each vertex representing the composition of a phase.

$$\mathrm{k} = \hat{\varphi}^{\mathcal{R}_i} - 1 \tag{14}$$

Examples include tie-lines in two-phase regions, tie-triangles in three-phase regions, tie-tetrahedra in four-phase regions, etc. In single-phase regions a "tie simplex" is a point, since there are not more than one phase to "tie together".

3.6. The Lever Rule

The phase fraction $x^{\sigma}_{\varphi_i}$ of any phase i present at equilibrium can be determined with tie simplices and the lever rule, which is based on the inverse distance principle. The closer the specified system composition $\mathbf{x}^{\sigma}_{\epsilon}$ is to the vertex $\mathbf{x}^{\varphi_i}_{\epsilon}$ of phase i in the tie simplex, the higher the fraction of phase i and the lower the fractions of the other phases.

When the system composition $\mathbf{x}^{\sigma}_{\epsilon}$ is inside a tie simplex $\Delta^{\mathcal{R}}$, it divides the tie simplex into $\hat{\varphi}$ phase-simplices $\Delta^{\mathcal{R}}_{\varphi_i}$, one for each phase i. The vertices of $\Delta^{\mathcal{R}}_{\varphi_i}$ include $\mathbf{x}^{\sigma}_{\epsilon}$ as well as all the vertices of $\Delta^{\mathcal{R}}$ except for $\mathbf{x}^{\varphi_i}_{\epsilon}$, the composition of phase i itself.

The phase fraction for a phase i in any $\hat{\varphi}$-phase region of any $\hat{\epsilon}$-component system is calculated with the generic lever rule, as shown in Equation (15). In single-phase regions, $x^{\sigma}_{\varphi_i} = 1$, since there is only one phase (and the content of a point is $\nu({}_0\Delta) = 1$).

$$x^{\sigma}_{\varphi_i} = \frac{\nu(\Delta^{\mathcal{R}}_{\varphi_i})}{\nu(\Delta^{\mathcal{R}})} \tag{15}$$

3.7. Calculating Thermochemical Properties

Once an equilibrium calculation is performed at temperature T and system composition $\mathbf{x}^{\sigma}_{\epsilon}$, the compositions $\mathbf{x}^{\varphi}_{\epsilon}$ of all phases and thermochemical quantities (e.g. H^{φ}, S^{φ}, G^{φ}) for each phase are known and can be stored. Now, for the same temperature T and any system composition $\mathbf{x}^{\sigma}_{\epsilon}$ inside the tie simplex, phase fractions $\mathbf{x}^{\sigma}_{\varphi}$ and system thermochemical properties (e.g. H^{σ}, S^{σ}, G^{σ}) can be calculated exactly with Equation (16) without performing another equilibrium calculation.

$$\tau^{\sigma} = \sum_{i=1}^{\hat{\varphi}} x^{\sigma}_{\varphi_i} \tau^{\varphi_i} \quad \text{where } \tau \in \{H, S, G, V\} \tag{16}$$

4. Demonstration of Foundational Concepts

In this section, the foundational concepts presented in the previous section is demonstrated by applying them to two- and three-component phase diagrams.

4.1. Two-component System

The isobaric CaO–SiO_2 system under ambient atmosphere shown in Figure 4a is presented as a two-component system example. Since pressure is constant, only one non-compositional potential is of concern, namely temperature; this means $\hat{\psi} = 1$. The system incorporates the chemical elements Ca, O, and Si; therefore $\hat{\varepsilon} = 3$. Due to the high oxygen potential of the ambient atmosphere, the oxygen content of the system is constrained to $n_{\mathrm{O}} = n_{\mathrm{Ca}} + 2n_{\mathrm{Si}}$. Therefore, a single system compositional constraint exist and $\hat{\zeta}^{\sigma} = 1$.

Calculating the phase diagram's dimensionality with Equation (6) yields $\mathbb{D}^{\sigma}_{\mathrm{g}} = 2$. The thermochemical system is therefore described with a 2D phase diagram. The axes of the phase diagram are the mole fraction of one system component x_{CaO} and temperature.

OPF region $\mathcal{B}^{\mathrm{sl}}_{\mathrm{sl}}$ has $\mathbb{D}^{\mathcal{B}} = (2{:}2{:}2)$. It is a 2D surface ($\mathbb{D}^{\mathcal{B}}_{\mathrm{g}} = 2$) with coordinates varying in both x_{CaO} and T ($\mathbb{D}^{\mathcal{B}}_{\mathrm{f}} = 2$), existing in a 2D phase diagram ($\mathbb{D}^{\sigma}_{\mathrm{g}} = 2$).

The two-phase $\mathcal{R}_{\mathrm{cr+sl}}$ region's $\mathcal{B}^{\mathrm{cr+sl}}_{\mathrm{cr}}$ boundary has $\mathbb{D}^{\mathcal{B}} = (1:1:2)$. $\mathbb{D}^{\mathcal{B}}_{\mathrm{g}} = \mathbb{D}^{\mathcal{B}}_{\mathrm{f}} = 1$ because it is a pure substance pinned to a single composition on the x_{CaO} axis. The $\mathcal{B}^{\mathrm{cr+sl}}_{\mathrm{sl}}$ boundary of this region has $\mathbb{D}^{\mathcal{B}} = (1{:}2{:}2)$. Although it is a 1D curve ($\mathbb{D}^{\mathcal{B}}_{\mathrm{g}} = 1$), its coordinates vary in both T and x_{CaO} and $\mathrm{f}^{\mathrm{sl}} = 2$, which yields $\mathbb{D}^{\mathcal{B}}_{\mathrm{f}} = 2$.

4.2. Three-component System

The isobaric CaO–MgO–SiO_2 system under ambient atmosphere shown in Figure 4b is presented as a three-component system example. With pressure constant, temperature is the only non-compositional potential, and $\hat{\psi} = 1$. The system involves the chemical elements Ca, Mg, O, and Si; therefore $\hat{\varepsilon} = 4$. A high oxygen potential again constrains the system oxygen content to $n_{\mathrm{O}} = n_{\mathrm{Ca}} + n_{\mathrm{Mg}} + 2n_{\mathrm{Si}}$. This single system compositional constraint yields $\hat{\zeta}^{\sigma} = 1$.

The phase diagram has $\mathbb{D}^{\sigma}_{\mathrm{g}} = 3$, which correctly indicates it to be 3-dimensional. The axes of the phase diagram are the mole fraction of two system components x_{CaO} and x_{MgO}, and temperature.

The $\mathcal{B}^{\mathrm{sl}}_{\mathrm{sl}}$ OPF region has $\mathbb{D}^{\mathcal{B}} = (3{:}3{:}3)$. It is a 3D volume ($\mathbb{D}^{\mathcal{B}}_{\mathrm{g}} = 3$) with coordinates varying with x_{CaO}, x_{MgO} and T ($\mathbb{D}^{\mathcal{B}}_{\mathrm{f}} = 3$), existing in a 3D phase diagram ($\mathbb{D}^{\sigma}_{\mathrm{g}} = 3$).

The two-phase $\mathcal{R}_{\mathrm{mw+sl}}$ region's $\mathcal{B}^{\mathrm{mw+sl}}_{\mathrm{mw}}$ boundary has $\mathbb{D}^{\mathcal{B}} = (1{:}1{:}3)$. Its geometric and functional dimensionalities are both equal to one, because it is a pure substance. The $\mathcal{B}^{\mathrm{mw+sl}}_{\mathrm{sl}}$ boundary of this region has $\mathbb{D}^{\mathcal{B}} = (2{:}3{:}3)$. Although it is a 2D curved surface ($\mathbb{D}^{\mathcal{B}}_{\mathrm{g}} = 2$), its coordinates vary with temperature and both composition coordinates, which yields $\mathbb{D}^{\mathcal{B}}_{\mathrm{f}} = 3$.

The two-phase $\mathcal{R}_{\mathrm{mt+sl}}$ region's $\mathcal{B}^{\mathrm{mt+sl}}_{\mathrm{mt}}$ boundary has $\mathbb{D}^{\mathcal{B}} = (2{:}2{:}3)$. Its geometric dimensionality is equal to two, because $\mathrm{f} = 2$ for the phase region, and $\mathrm{f}^{\mathrm{mt}} = 2$ for this phase. $\mathbb{D}^{\mathcal{B}}_{\mathrm{f}} = 2$ because the phase only exists on the line connecting the Ca_2SiO_4 and Mg_2SiO_4 end members.

Because f = 1 in the three-phase $\mathcal{R}_{\text{mw+mt+sl}}$ region, $\mathbb{D}_{\text{g}}^{\mathcal{B}} = 1$ for all three phases. For the merwinite boundary $\mathbb{D}_{\text{f}}^{\mathcal{B}} = 1$, since it is a pure substance. For the monticellite boundary $\mathbb{D}_{\text{f}}^{\mathcal{B}} = 2$ since the phase exists on the line connecting the Ca_2SiO_4 and Mg_2SiO_4 end members and therefore $\text{f}^{\text{mt}} = 2$. Finally, $\mathbb{D}_{\text{f}}^{\mathcal{B}} = 3$ for the slag boundary because this phase has no additional compositional constraints beyond those of the system.

4.3. General System

The method employed here to two- and three-component systems applies to $\hat{\epsilon}$-component systems in general. This, along with the generality of simplex geometry, the Cayley-Menger determinant, and the generic lever rule, provides a general basis for discretization and interpolation of OPF regions and boundaries, and for the calculation of phase fractions, phase compositions, and thermochemical properties.

5. Acceleration Algorithm

5.1. Overview

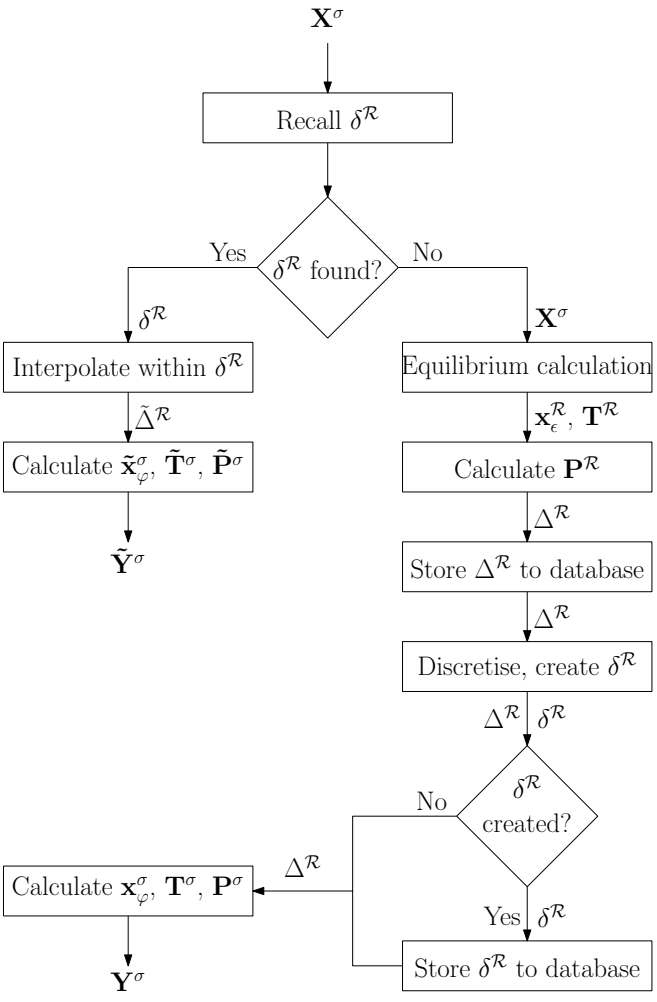

Figure 6: High-level flow diagram of the accelerator algorithm.

Figure 6 provides a high-level overview of the accelerator algorithm. When a model requires an equilibrium state $\mathbf{Y}^\sigma$ at a specified system state $\mathbf{X}^\sigma$, the accelerator searches its database for a phase region cell $\delta^{\mathcal{R}}$ that contains $\mathbf{X}^\sigma$. If a phase region cell is found, it is used to create an interpolated tie simplex $\tilde{\Delta}^{\mathcal{R}}$ that describes the equilibrium states of the phases. The lever rule (Equation (15)) and Equation (16) are then used to calculate an interpolated system equilibrium state $\tilde{\mathbf{Y}}^\sigma$.

When a phase region cell is not found, a direct calculation is performed and a tie simplex $\Delta^{\mathcal{R}}$ is created and stored in the database. An attempt is then made to create a new phase region cell from all stored tie simplices. If successful, the new cell is stored for later recall. Thereafter, the directly calculated system equilibrium state $\mathbf{Y}^\sigma$ is returned to the model.

The algorithm concept is generic, and is presented here for arbitrary numbers of independent system components $\hat{\epsilon}$ and non-compositional potentials $\hat{\psi}$. Its current implementation includes temperature as the only non-compositional potential, however. The algorithm is divided into three routines; (1) discretisation, (2) interpolation, and (3) storage and recall.

5.2. Discretisation

Figure 7 shows an overview of the algorithm's discretisation routine. The purpose of this routine is to discretise features of a system's phase diagram and create discrete finite regions of the phase diagram that can be used in the interpolation routine. Firstly, the features of a system's phase diagram that needs to be discretised, has to be identified. Thereafter can the discretisation of these features and the creation of discrete finite regions be discussed.

Features to Discretise. The lever rule allows for the calculation of phase fractions, thermochemical properties and some physical properties at any specified state within a multi-phase region. Therefore, only OPF features $\mathcal{B}$, as shown in Figure 4, are discretised, rather than entire multi-phase regions. This reduces the number of direct equilibrium calculations required to cover a phase region, and the amount of data that need to be stored, in comparison with previous methods that discretise entire phase regions [5]. For some physical properties, such as viscosity, additional material property models are required to determine the property values from the calculated or interpolated system equilibrium state.

Boundary Discretisation with Simplices. The algorithm uses k-simplices to discretise kD OPF boundaries. A single simplex is referred to as a discretisation segment $\delta^{\mathcal{B}}$ of boundary $\mathcal{B}$. It has at least $\mathbb{D}_{\text{g}}^{\mathcal{B}} + 1$ vertices, and therefore requires this number of direct equilibrium calculations.

The OPF boundary $\mathcal{B}_{\text{j}}^{\text{i}}$ of phase j that has the highest geometrical dimensionality in phase region $\mathcal{R}_{\text{i}}$ determines

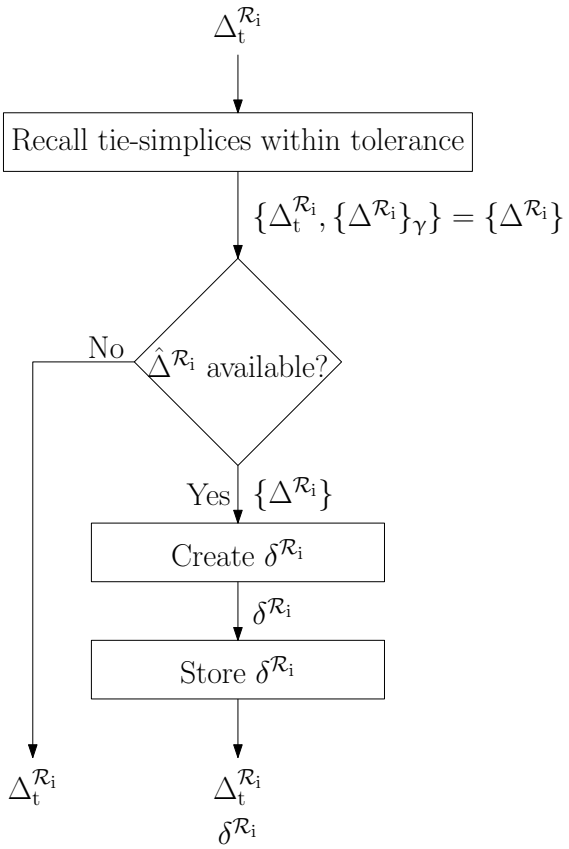

Figure 7: Flow diagram of discretisation routine.

the number of tie simplices $\hat{\Delta}^{\mathcal{R}_i}$ that must be directly calculated to create one complete discretisation segment $\delta^{\mathcal{B}_j^i}$ on each boundary. This is calculated with Equation (17).

$$\hat{\Delta}^{\mathcal{R}_i} = \max(\mathbb{D}_g^{\mathcal{B}_1^i}, \ldots, \mathbb{D}_g^{\mathcal{B}_\varphi^i}) + 1 \tag{17}$$

For example, consider a two-phase region with a 1D OPF boundary and a 2D OPF boundary. The 1D boundary will require a line segment (2 vertices) and the 2D boundary will require a triangle (3 vertices) to generate one complete OPF boundary discretisation segment on each. Three equilibrium calculations are therefore required to generate three tie-lines, to generate a triangle on the 2D OPF boundary. This will yield three vertices on the 1D boundary, which is more than the minimum of two that is required to produce a line segment.

Phase Region Cell. A new tie simplex $\Delta_t^{\mathcal{R}_i}$ is created when a direct equilibrium calculation is performed. The database is then queried for all tie simplices $\{\Delta^{\mathcal{R}_i}\}_\gamma$ that are within the specified temperature and composition tolerances ($\Delta T^{\mathcal{D}}$ and $\Delta x_\epsilon^{\mathcal{D}}$) from $\Delta_t^{\mathcal{R}_i}$. The tolerances allow control over the magnitude of interpolation errors. If $\hat{\Delta}^{\mathcal{R}_i}$ tie simplices are available, they are combined to form a phase region cell $\delta^{\mathcal{R}_i}$ that discretises a finite portion of $\mathcal{R}_i$. Example phase region cells are shown in Figure 8 for two- and three-component systems. To cover further portions of $\mathcal{R}_i$, more phase region cells are constructed by creating additional tie simplices through direct equilibrium calculations.

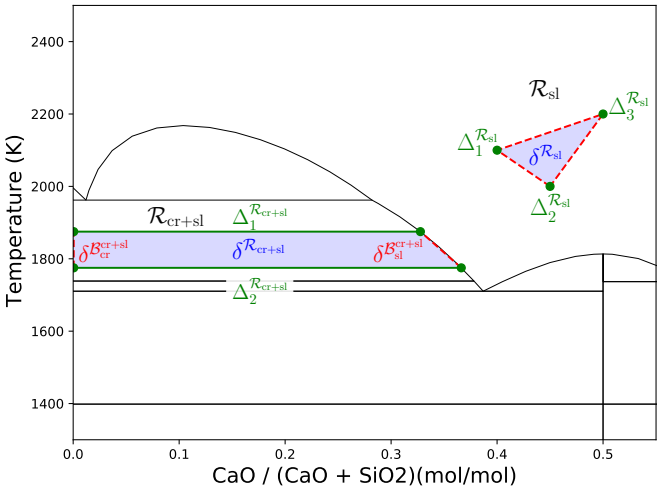

(a) Phase region cells in single and two-phase regions in the CaO–SiO_2 two-component system. (sl: slag, cr: cristobalite)

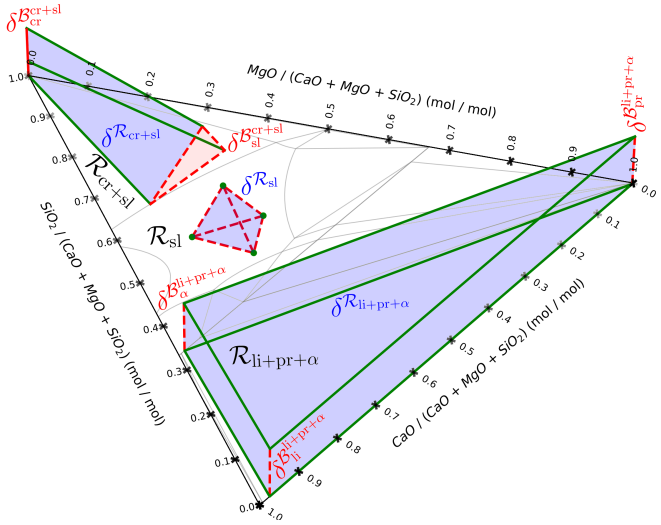

(b) Phase region cells in single, two-phase, and three-phase regions in the CaO–MgO–SiO_2 three-component system. (sl: slag, cr: cristobalite, li: lime, pr: periclase, α: α-Ca_2SiO_4). The vertical axis (not indicated) is the temperature axis.

Figure 8: Phase region cells in two- and three-component systems.

5.3. Interpolation

To calculate an interpolated equilibrium state $\tilde{\mathbf{Y}}^\sigma$ for a specified system state $\mathbf{X}^\sigma$ from a phase region cell $\delta^{\mathcal{R}_i}$, an interpolated tie simplex $\tilde{\Delta}^{\mathcal{R}_i}$ is created. This employs two interpolation steps, as shown in Figure 9; interpolation (1) to the non-compositional potentials $\mathbf{\Psi}^\sigma$ in $\mathbf{X}^\sigma$ and (2) to the chemical potentials $\boldsymbol{\mu}_\epsilon^\sigma$ corresponding to $\mathbf{X}^\sigma$.

Interpolation to $\mathbf{\Psi}^\sigma$. When interpolating to $\mathbf{\Psi}^\sigma$, the degrees of freedom, geometric dimensionality of the OPF boundaries, and consequently the number of tie simplices required to discretise the boundaries $\hat{\Delta}_\psi^{\mathcal{R}_i}$, are reduced

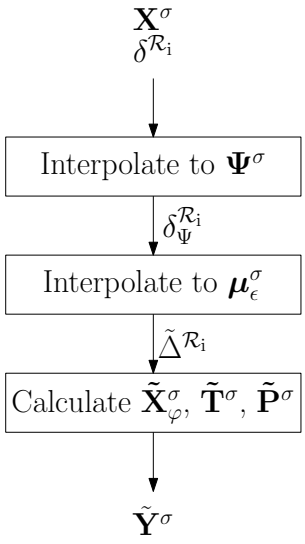

Figure 9: Interpolation routine flow diagram.

by $\hat{\psi}$, as shown in Equation (18). This yields an iso-non-compositional-potential (iso-ψ) section $\delta^{\mathcal{R}_\mathrm{i}}_\psi$ through $\delta^{\mathcal{R}_\mathrm{i}}$, consisting of $\hat{\Delta}^{\mathcal{R}_\mathrm{i}}_\psi$ interpolated iso-ψ tie simplices $\tilde{\Delta}^{\mathcal{R}_\mathrm{i}}_\psi$.

$$\hat{\Delta}^{\mathcal{R}}_\psi = \hat{\Delta}^{\mathcal{R}} - \hat{\psi} \tag{18}$$

Figure 10a shows an example phase region cell in a three-component two-phase region consisting of three tie simplices ($\hat{\Delta}^{\mathcal{R}} = 3$). When an iso-ψ section $\delta^{\mathcal{R}_\mathrm{i}}_\psi$ is created through the phase region cell at the system temperature ($\hat{\psi} = 1$), two interpolated iso-ψ tie simplices ($\hat{\Delta}^{\mathcal{R}}_\psi = 2$) are produced. These tie simplices create an iso-ψ discretisation segment $\delta^{\mathcal{B}}_\psi$ on each OPF boundary.

Phase regions where $\hat{\mathrm{e}} - \hat{\zeta}^\sigma = \hat{\varphi}$ have degrees of freedom $\mathrm{f} = \hat{\psi}$. In these cases, interpolating to $\mathbf{\Psi}^\sigma$ within a phase region cell yields only one iso-ψ tie simplex, which can be used as the final interpolated tie simplex $\tilde{\Delta}^{\mathcal{R}}$.

Interpolation to $\boldsymbol{\mu}^\sigma_\epsilon$. Although the iso-ψ tie simplices $\tilde{\Delta}^{\mathcal{R}_\mathrm{i}}_\psi$ shown in Figure 10a, as well as all other tie simplices within $\delta^{\mathcal{R}_\mathrm{i}}_\psi$ have the same non-compositional potentials $\mathbf{\Psi}^\sigma$, they have different chemical potentials, as seen in Figure 10b. Somewhere within the iso-ψ section through the phase region cell $\delta^{\mathcal{R}_\mathrm{i}}_\psi$ there exists a tie simplex, referred to as the interpolated tie simplex $\tilde{\Delta}^{\mathcal{R}}$, that contains the system composition and thus have the same chemical potentials $\boldsymbol{\mu}^\sigma_\epsilon$ as the specified state, seen in Figure 10b,. Therefore, the objective of this interpolation step is to find the phase compositions $\tilde{\mathbf{x}}^\varphi_\epsilon(\mathbf{\Psi}^\sigma, \boldsymbol{\mu}^\sigma_\epsilon)$ that correspond to the vertices of the interpolated tie simplex $\tilde{\Delta}^{\mathcal{R}}$ that perfectly contains the system composition $\mathbf{x}^\sigma_\epsilon$.

As seen in Figure 10c, iso-ψ boundary discretisation segment barycentric coordinate weights $\boldsymbol{\beta}^{\mathcal{B}}_\mathrm{i}$ can be used to express the composition of phase i of the interpolated tie simplex $\tilde{\mathbf{x}}^{\varphi_\mathrm{i}}_\epsilon(\mathbf{\Psi}^\sigma, \boldsymbol{\mu}^\sigma_\epsilon)$ as a function of $\hat{\Delta}^{\mathcal{R}}_\psi$ iso-ψ boundary discretisation segment phase compositions

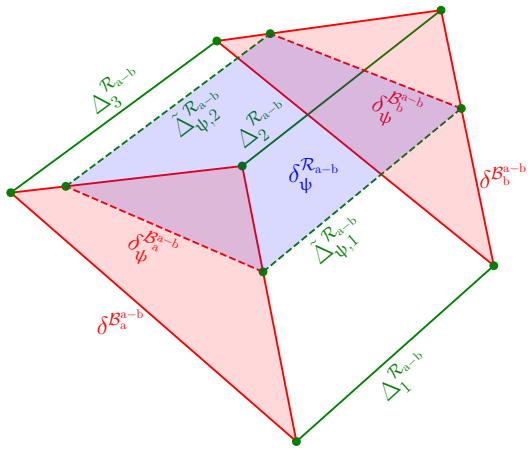

(a) A phase region cell $\delta^{\mathcal{R}_{a\text{-}b}}$ in two-phase region $\mathcal{R}_{a\text{-}b}$ in a three-component system where phases a and b are stable, with phase boundary segments $\delta^{\mathcal{B}^{a\text{-}b}_i}$ and $\delta^{\mathcal{B}^{a\text{-}b}_b}$ (shaded in red) and tie simplices $\Delta^{\mathcal{R}_{a-b}}$, (solid green). An iso-ψ section $\delta^{\mathcal{R}_{a\text{-}b}}_\psi$ (shaded in blue) is made through the phase region cell and is bounded by interpolated iso-ψ tie simplices $\tilde{\Delta}^{\mathcal{R}_{a\text{-}b}}_\psi$ (dashed green) and discretisation segments $\delta^{\mathcal{B}^{a\text{-}b}_a}_\psi$ and $\delta^{\mathcal{B}^{a\text{-}b}_b}_\psi$ (dashed red).

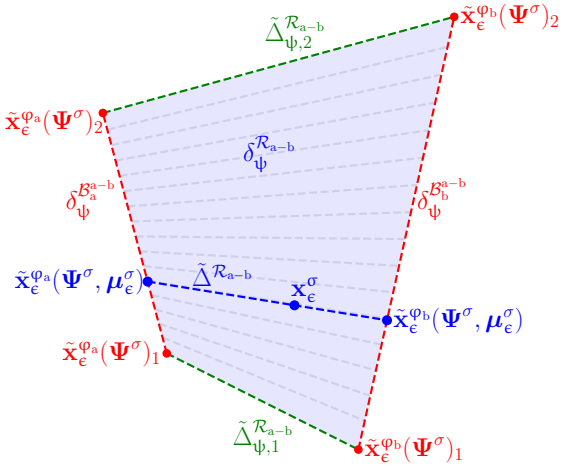

(b) Iso-ψ section $\delta^{\mathcal{R}_{a\text{-}b}}_\psi$ with tie simplices at different chemical potentials indicated with grey dashed lines and the interpolated tie simplex $\tilde{\Delta}^{\mathcal{R}_{a\text{-}b}}$ (dashed blue) at $\boldsymbol{\mu}^\sigma_\epsilon$, perfectly containing $\mathbf{x}^\sigma_\epsilon$.

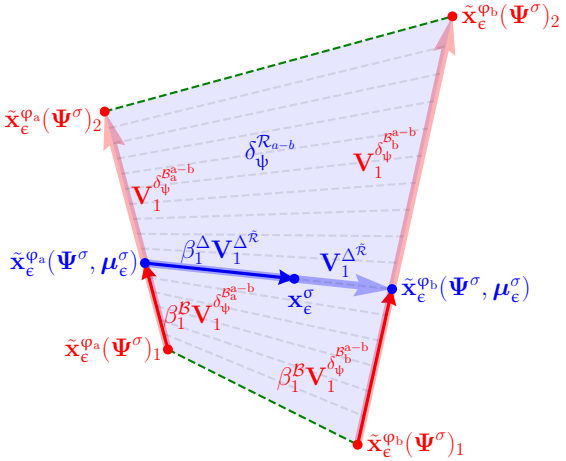

(c) Vectors and barycentric coordinate weights used to describe $\mathbf{x}^\sigma_\epsilon$ as a function of all the $\tilde{\mathbf{x}}^\varphi_\epsilon(\mathbf{\Psi}^\sigma)$

Figure 10: Phase region cell interpolation steps in a two-phase region in a three-component system.

$\tilde{\mathbf{x}}_\epsilon^{\varphi_i}(\boldsymbol{\Psi}^\sigma)$. This expression can be seen in Equation (19). Because there are $\hat{\Delta}_\psi^\mathcal{R}$ iso-ψ boundary discretisation segment phase compositions $\tilde{\mathbf{x}}_\epsilon^\varphi(\boldsymbol{\Psi}^\sigma)$, only $\hat{\Delta}_\psi^\mathcal{R} - 1$ iso-ψ boundary discretisation segment barycentric coordinate weights $\beta^\mathcal{B}$ are required in $\boldsymbol{\beta}_i^\mathcal{B}$ to express the composition of phase i of the interpolated tie simplex $\tilde{\mathbf{x}}_\epsilon^{\varphi_i}(\boldsymbol{\Psi}^\sigma, \boldsymbol{\mu}_\epsilon^\sigma)$.

$$\tilde{\mathbf{x}}_\epsilon^{\varphi_i}(\boldsymbol{\Psi}^\sigma, \boldsymbol{\mu}_\epsilon^\sigma) = \tilde{\mathbf{x}}_\epsilon^{\varphi_i}(\boldsymbol{\Psi}^\sigma)_1 + \sum_{j=2}^{\hat{\Delta}_\psi^\mathcal{R}} \beta_{j-1}^\mathcal{B} \left(\tilde{\mathbf{x}}_\epsilon^{\varphi_i}(\boldsymbol{\Psi}^\sigma)_j - \tilde{\mathbf{x}}_\epsilon^{\varphi_i}(\boldsymbol{\Psi}^\sigma)_1\right) \tag{19}$$

It is assumed that system component chemical potentials vary linearly between the phase composition coordinates of an iso-ψ boundary discretisation segment $\delta_\psi^\mathcal{B}$, as seen in Figures 10b and 10c. This assumption is reasonable when temperature and composition tolerances ($\Delta T^\mathcal{D}$ and $\Delta x_\epsilon^\mathcal{D}$) are sufficiently small. The assumption results in the set of iso-ψ boundary discretisation segment barycentric coordinate weights of all iso-ψ boundary discretisation segments being identical, as shown in Equation (20).

$$\boldsymbol{\beta}_1^\mathcal{B} = \cdots = \boldsymbol{\beta}_{\hat{\varphi}}^\mathcal{B} = \boldsymbol{\beta}^\mathcal{B} = [\beta_1^\mathcal{B}, \ldots, \beta_{\hat{\Delta}_\psi^\mathcal{R}-1}^\mathcal{B}] \tag{20}$$

Equation (19) only provides an expression of a phase composition contained within a iso-ψ boundary discretisation segment $\delta_\psi^\mathcal{B}$ – varying $\boldsymbol{\beta}^\mathcal{B}$ changes the location of these phase compositions on each iso-ψ boundary discretisation segment. These phase compositions have to be coupled to the system composition $\mathbf{x}_\epsilon^\sigma$ in order to determine the exact phase compositions that correspond to the chemical potential of the system composition.

Tie simplex barycentric coordinate weights $\boldsymbol{\beta}^\Delta$ can be used to express the specified system composition $\mathbf{x}_\epsilon^\sigma$ as a function of each of the $\hat{\varphi}$ phase compositions $\tilde{\mathbf{x}}_\epsilon^\varphi(\boldsymbol{\Psi}^\sigma, \boldsymbol{\mu}_\epsilon^\sigma)$, as shown in Figure 10c. This expression is shown in Equation (21). An interpolated tie simplex that perfectly contains the system composition $\mathbf{x}_\epsilon^\sigma$ can be obtained if the conditions in Equation (13) are satisfied for all tie simplex barycentric coordinate weights in $\boldsymbol{\beta}^\Delta$. Because there are $\hat{\varphi}$ number of phases present in a tie simplex, $\hat{\varphi} - 1$ number of tie simplex barycentric coordinate weights are required to express the system composition $\mathbf{x}_\epsilon^\sigma$.

$$\mathbf{x}_\epsilon^\sigma = \tilde{\mathbf{x}}_\epsilon^{\varphi_1}(\boldsymbol{\Psi}^\sigma, \boldsymbol{\mu}_\epsilon^\sigma) + \sum_{i=2}^{\hat{\varphi}} \beta_{i-1}^\Delta \left(\tilde{\mathbf{x}}_\epsilon^{\varphi_i}(\boldsymbol{\Psi}^\sigma, \boldsymbol{\mu}_\epsilon^\sigma) - \tilde{\mathbf{x}}_\epsilon^{\varphi_1}(\boldsymbol{\Psi}^\sigma, \boldsymbol{\mu}_\epsilon^\sigma)\right) \tag{21}$$

With the interpolated tie simplex's phase compositions $\tilde{\mathbf{x}}_\epsilon^\varphi(\boldsymbol{\Psi}^\sigma, \boldsymbol{\mu}_\epsilon^\sigma)$ expressed in terms of iso-ψ boundary discretisation segment phase compositions $\tilde{\mathbf{x}}_\epsilon^\varphi(\boldsymbol{\Psi}^\sigma)$ and barycentric coordinate weights $\boldsymbol{\beta}^\mathcal{B}$ with Equation (19), the barycentric coordinate weights $\boldsymbol{\beta}^\mathcal{B}$ have to be solved that satisfy the conditions of Equation (13) for all tie simplex barycentric coordinate weights in $\boldsymbol{\beta}^\Delta$.

An expression for each of the interpolated tie simplex's $\hat{\varphi}$ phase compositions $\tilde{\mathbf{x}}_\epsilon^\varphi(\boldsymbol{\Psi}^\sigma, \boldsymbol{\mu}_\epsilon^\sigma)$ is created with Equation (19) and substituted into Equation (21). This creates an expression of the system composition $\mathbf{x}_\epsilon^\sigma$ as a function of each iso-ψ boundary discretisation segment's phase compositions $\tilde{\mathbf{x}}_\epsilon^\varphi(\boldsymbol{\Psi}^\sigma)$ and barycentric coordinate weights $\boldsymbol{\beta}^\Delta$ and $\boldsymbol{\beta}^\mathcal{B}$. This expression is factorised and written as a set of non-linear equations, shown in Equation (22), with vectors and matrices with sizes as follow:

$\mathbf{x}_\epsilon^\sigma$ **:** $\hat{\epsilon} \times 1$ vector of the system composition.

$\mathbf{B}$ **:** $\hat{\epsilon} \times (\hat{\Delta}_\psi^\mathcal{R} \times \hat{\varphi})$ matrix of the iso-ψ boundary discretisation segment phase compositions.

$\mathbf{w}$ **:** $(\hat{\Delta}_\psi^\mathcal{R} \times \hat{\varphi}) \times 1$ vector of barycentric coordinate weight expressions.

$$\mathbf{x}_\epsilon^\sigma = \mathbf{B}\mathbf{w} \tag{22}$$

$$\mathbf{B} = \begin{bmatrix} \tilde{\mathbf{x}}_{\epsilon_{(\psi)}}^{\mathcal{B}_1^i} & \ldots & \tilde{\mathbf{x}}_{\epsilon_{(\psi)}}^{\mathcal{B}_{\hat{\varphi}}^i} \end{bmatrix} \tag{23}$$

$$\tilde{\mathbf{x}}_{\epsilon_{(\psi)}}^{\mathcal{B}_i} = \begin{bmatrix} \tilde{\mathbf{x}}_{\epsilon_1}^{\varphi_i} \ldots \tilde{\mathbf{x}}_{\epsilon_{\hat{\Delta}^\mathcal{R}\psi-1}}^{\varphi_i} \end{bmatrix} \tag{24}$$

$$\mathbf{w} = \begin{bmatrix} (1-\Sigma\boldsymbol{\beta}^\mathcal{B})(1-\Sigma\boldsymbol{\beta}^\Delta) \\ (\beta_1^\mathcal{B})(1-\Sigma\boldsymbol{\beta}^\Delta) \\ \vdots \\ (\beta_{\hat{\Delta}_\psi^\mathcal{R}-1}^\mathcal{B})(1-\Sigma\boldsymbol{\beta}^\Delta) \\ \hline (1-\Sigma\boldsymbol{\beta}^\mathcal{B})(\beta_1^\Delta) \\ (\beta_1^\mathcal{B})(\beta_1^\Delta) \\ \vdots \\ (\beta_{\hat{\Delta}_\psi^\mathcal{R}-1}^\mathcal{B})(\beta_1^\Delta) \\ \hline \vdots \\ \hline (1-\Sigma\boldsymbol{\beta}^\mathcal{B})(\beta_{\hat{\varphi}-1}^\Delta) \\ (\beta_1^\mathcal{B})(\beta_{\hat{\varphi}-1}^\Delta) \\ \vdots \\ (\beta_{\hat{\Delta}_\psi^\mathcal{R}-1}^\mathcal{B})(\beta_{\hat{\varphi}-1}^\Delta) \end{bmatrix} \tag{25}$$

$$\Sigma\boldsymbol{\beta}^\Delta = \sum_{i=1}^{\hat{\varphi}-1} \beta_i^\Delta : \beta_i^\Delta \in \mathbb{R}[0,1] \tag{26}$$

$$\Sigma\boldsymbol{\beta}^\mathcal{B} = \sum_{j=1}^{\hat{\Delta}_\psi^\mathcal{R}-1} \beta_j^\mathcal{B} : \beta_j^\mathcal{B} \in \mathbb{R}[0,1] \tag{27}$$

This set of non-linear equations is solved iteratively to obtain barycentric coordinate weight vector $\mathbf{w}$ and with it, the $\boldsymbol{\beta}^{\mathcal{B}}$ barycentric coordinate weights that relate to phase compositions of an interpolated tie simplex $\tilde{\mathbf{x}}_{\epsilon}^{\varphi}(\boldsymbol{\Psi}^{\sigma}, \boldsymbol{\mu}_{\epsilon}^{\sigma})$ through Equation (19) that perfectly contains the system's composition. The physical and thermochemical properties of each phase can then be calculated and the complete interpolated tie simplex $\tilde{\Delta}^{\mathcal{R}}$ has been obtained.

The iterative solving of a non-linear system of equations is not desired when attempting to accelerate equilibrium equations. An explicit expression would be preferred, but no such generic explicit expression could yet be derived or found in literature. This is the most critical part of the algorithm that has to be addressed to improve on efficiency and performance.

Calculate the Interpolated Equilibrium State. With the interpolated tie simplex $\tilde{\Delta}^{\mathcal{R}}$ calculated, the lever rule is used to calculate phase fractions $\tilde{\mathbf{x}}_{\varphi}^{\sigma}$ at the specified system composition $\mathbf{x}_{\epsilon}^{\sigma}$ and in turn are used to calculate the physical and thermochemical properties of the system. This yields the interpolated equilibrium state $\tilde{\mathbf{Y}}^{\sigma}$.

5.4. Storage and Recall

The in-situ approach to populate the database with tie simplices and phase region cells is inherently unstructured; data is generated and stored at temperatures and phase compositions that have no fixed intervals. Searching through such unstructured data is inefficient, which leads to extended searching times. An efficient storage and recall algorithm is therefore needed.

A Structured Reference Frame. To configure the accelerator, limits and tolerances are specified for all non-compositional potentials, and for each system component. Taking temperature as an example, the limits are $T_{\min}^{\mathcal{D}}$ and $T_{\max}^{\mathcal{D}}$, and the tolerance is $\Delta T^{\mathcal{D}}$. In the case of composition, for all system components limits of zero and one are used and a single tolerance $\Delta x_{\epsilon}^{\mathcal{D}}$ is specified.

The specified limits and tolerances define a structured and uniform reference frame that covers the system's phase diagram, $\mathcal{D}$, as illustrated in Figure 11a. The size of each reference frame cell $\delta^{\mathcal{D}}$ is equal to the specified tolerances. Cells are identified with a non-compositional potential index array $\mathbf{I}^{\boldsymbol{\Psi}}$ and a composition index array $\mathbf{I}^{\epsilon}$, with index values calculated according to Equations (28) and (29).

$$\iota_T = \text{floor}\left(\frac{T^{\sigma} - T_{\min}^{\mathcal{D}}}{\Delta T^{\mathcal{D}}}\right) \tag{28}$$

$$\iota_{x_\epsilon} = \text{floor}\left(\frac{x_{\epsilon}^{\sigma}}{\Delta x_{\epsilon}^{\mathcal{D}}}\right) \tag{29}$$

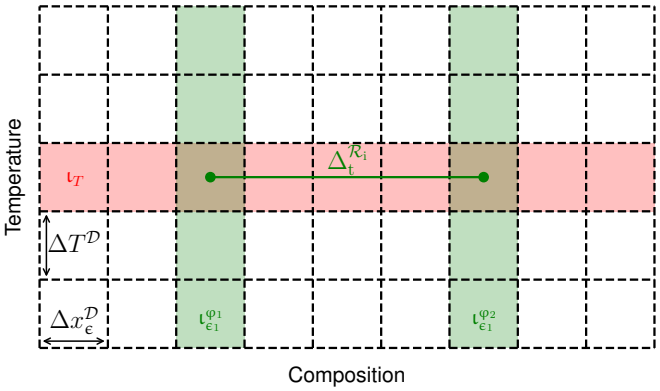

(a) Structured reference frame indicating the non-compositional potential index ι_T of temperature and composition indices of each phase $\iota_{\epsilon}^{\varphi}$ of tie simplex $\Delta_{\mathrm{t}}^{\mathcal{R}_{\mathrm{i}}}$.

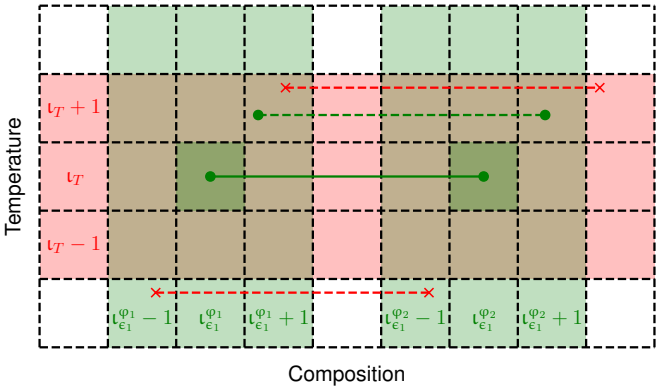

(b) Valid reference frame cell ranges of a newly created tie simplex $\Delta_{\mathrm{t}}^{\mathcal{R}_{\mathrm{i}}}$ (solid green) and example of a valid tie simplex (dashed green) that can be used to possibly create a phase region cell and examples of invalid tie simplices (dashed red).

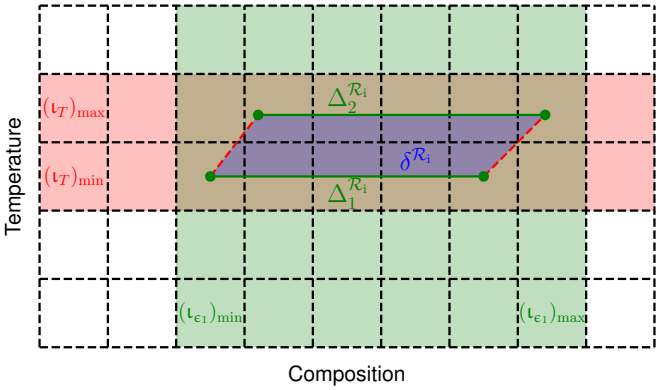

(c) Reference frame cell ranges of compositional and non-compositional potential indices that fully contain the phase region cell $\delta^{\mathcal{R}_{\mathrm{i}}}$.

Figure 11: Reference frame cells that are used in the storage and recall of tie simplices and phase region cells.

Storing Tie Simplices. Figure 12 shows the flow diagram of the tie simplex storing routine. When a tie simplex is created, the ID of the phase region its found within $\mathcal{R}_{\mathrm{i}}$ is determined. All tie simplices found in this phase region will have the same phase region ID. Thereafter, a unique tie simplex ID, t, is assigned to it.

The non-compositional potential index array $\mathbf{I}^{\boldsymbol{\Psi}}$ of the tie simplex is determined and then, for each of the

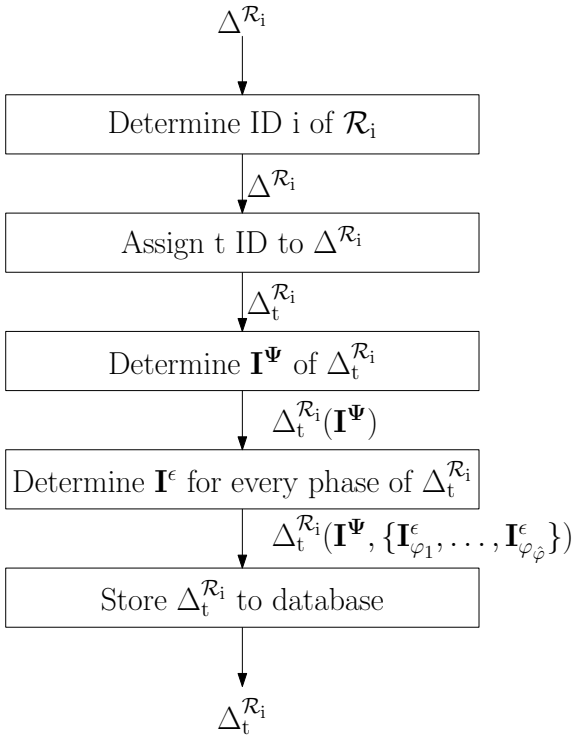

Figure 12: Tie-simplex storage routine flow diagram.

tie simplex's $\hat{\varphi}$ phases, the composition index array $\mathbf{I}^{\epsilon}$ in the structured reference frame is determined. Each of the phases' $\mathbf{I}^{\epsilon}$ in combination with the tie simplex's $\mathbf{I}^{\Psi}$ refers to a single cell in the structured reference frame $\delta^{\mathcal{D}}$, as shown in Figure 11a.

The complete description of the tie simplex is; (1) the tie simplex ID t, (2) the phase region ID $\mathcal{R}_i$, (3) the non-compositional potential index array $\mathbf{I}^{\Psi}$ of the tie simplex, and (4) the composition index array for each of the $\hat{\varphi}$ phases $\{\mathbf{I}^{\epsilon}_{\varphi_1}, \ldots, \mathbf{I}^{\epsilon}_{\varphi_{\hat{\varphi}}}\}$. The tie simplex, together with its complete description, is stored to the database.

Tie Simplices Within Tolerance. Because interpolation is done between tie simplices to create an interpolated tie simplex, errors can be made with phase compositions, as shown in Figure 13, but also with physical and thermochemical properties of the phases.

To control the interpolation error magnitude, only tie simplices that are within the specified temperature tolerance $\Delta T^{\mathcal{D}}$ and composition tolerance $\Delta x_{\epsilon}^{\mathcal{D}}$ are used to create a phase region cell. The temperature tolerance is enforced by determining the difference between two tie simplices' temperatures, shown in Equation (30). The composition tolerance is enforced by determining the distance between the compositions of the same phase of two tie simplices, shown in Equation (31).

$$\left| T^{\Delta_i^{\mathcal{R}}} - T^{\Delta_j^{\mathcal{R}}} \right| <= \Delta T^{\mathcal{D}} \tag{30}$$

$$\left| \mathbf{x}_{\epsilon}^{\varphi_k \Delta_i^{\mathcal{R}}} - \mathbf{x}_{\epsilon}^{\varphi_k \Delta_j^{\mathcal{R}}} \right| <= \Delta x_{\epsilon}^{\mathcal{D}} \tag{31}$$

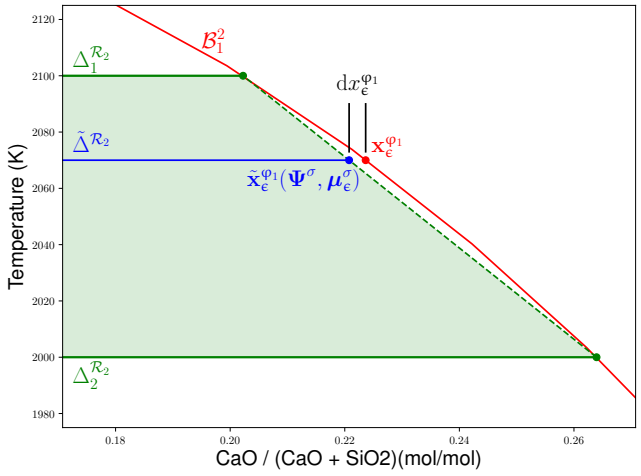

Figure 13: Illustration of error that can be made when linear interpolation is performed to obtain the phase composition $\tilde{\mathbf{x}}_{\epsilon}^{\varphi_1}(\boldsymbol{\Psi}^{\sigma}, \boldsymbol{\mu}_{\epsilon}^{\sigma})$ of an interpolated tie simplex $\tilde{\Delta}^{\mathcal{R}_2}$ from two tie simplices $\Delta_1^{\mathcal{R}_2}$ and $\Delta_2^{\mathcal{R}_2}$. Its for this reason that discretisation tolerances are introduced. The temperature and composition tolerances depicted here are much larger than what would normally be specified, for illustration purposes.

When two tie simplices are within $\Delta T^{\mathcal{D}}$ from one another and each of their phases are within $\Delta x_{\epsilon}^{\mathcal{D}}$ from one another are they considered to be close enough to be included into a phase region cell.

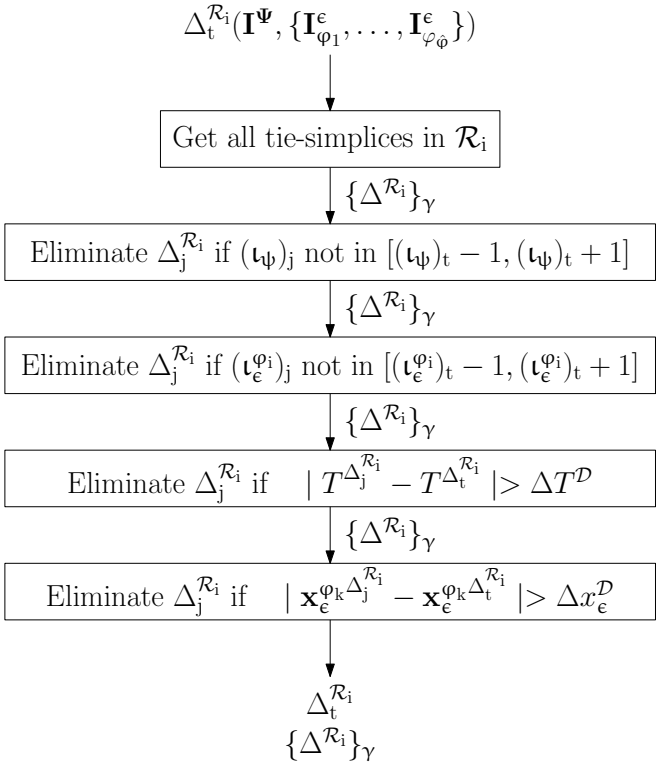

Figure 14: Tie-simplex recall routine flow diagram.

Recalling Tie Simplices. Figure 14 shows the flow diagram of the tie simplex recall routine. An equilibrium calculation is performed and a new tie simplex $\Delta_{\mathrm{t}}^{\mathcal{R}_{\mathrm{i}}}$ created and stored, as discussed. A number of tie simplices surrounding the newly created tie simplex has to be found that are within tolerance, and then recalled to create a phase region cell.

The phase region to which the new tie simplex belong $\mathcal{R}_{\mathrm{i}}$ is known, and only the stored tie simplices belonging to the same phase region has to be considered. This filter is applied and a list of eligible tie simplices returned $\{\Delta^{\mathcal{R}_{\mathrm{i}}}\}_{\gamma}$.

Because the cell sizes of the reference frame is driven by the specified tolerances, only the set of reference frame cells surrounding the new tie simplex have to be searched. Anything further would automatically not be within tolerance, as shown in Figure 11b.

A tie simplex has $\hat{\psi}$ of non-compositional potential indices; $(\iota_{\psi})_{\mathrm{t}}$ refers to the new tie simplex and $(\iota_{\psi})_{\mathrm{j}}$ to a tie simplex in the recall set $\{\Delta^{\mathcal{R}_{\mathrm{i}}}\}_{\gamma}$. Only when all of a tie simplex's non-compositional potential indices $(\iota_{\psi})_{\mathrm{j}}$ are within the same or neighbouring non-compositional potential indices as the new tie simplex $(\iota_{\psi})_{\mathrm{t}}$, as expressed in Equation (32) and illustrated in Figure 11b, is the tie simplex considered further. Otherwise its eliminated from the recall set $\{\Delta^{\mathcal{R}_{\mathrm{i}}}\}_{\gamma}$.

Each of the $\hat{\varphi}$ number of phases of a tie simplex have $\hat{\epsilon}$ of chemical potentials indices; $(\iota_{x_{\epsilon}}^{\varphi_{\mathrm{i}}})_{\mathrm{t}}$ refers to phase i of the new tie simplex and $(\iota_{x_{\epsilon}}^{\varphi_{\mathrm{i}}})_{\mathrm{j}}$ of a tie simplex in the recall set $\{\Delta^{\mathcal{R}_{\mathrm{i}}}\}_{\gamma}$. Only when each phase's chemical potential indices $(\iota_{x_{\epsilon}}^{\varphi_{\mathrm{i}}})_{\mathrm{j}}$ of a tie simplex are within the same or neighbouring non-compositional potential indices as the new tie simplex $(\iota_{x_{\epsilon}}^{\varphi_{\mathrm{i}}})_{\mathrm{t}}$, as expressed in Equation (33) and illustrated in Figure 11b, is the tie simplex considered further. Otherwise its eliminated from the recall set $\{\Delta^{\mathcal{R}_{\mathrm{i}}}\}_{\gamma}$.

$$(\iota_{\psi})_{\mathrm{j}} \in [(\iota_{\psi})_{\mathrm{t}} - 1, (\iota_{\psi})_{\mathrm{t}} + 1] \tag{32}$$

$$(\iota_{x_{\epsilon}}^{\varphi_{\mathrm{i}}})_{\mathrm{j}} \in \left[(\iota_{x_{\epsilon}}^{\varphi_{\mathrm{i}}})_{\mathrm{t}} - 1, (\iota_{x_{\epsilon}}^{\varphi_{\mathrm{i}}})_{\mathrm{t}} + 1\right] \tag{33}$$

This is computationally cheap way of reducing the number of tie simplices that have to be investigated to confirm whether they are within tolerance. Each of the tie simplices in the list $\{\Delta^{\mathcal{R}_{\mathrm{i}}}\}_{\gamma}$ that passed the reference frame check are now investigated if they are in fact within the temperature tolerance with Equation (30) and eliminated from the list if they fail. The remaining tie simplices are investigated to confirm whether each of their phases are within compositional tolerance with the new tie simplex with Equation (31) and eliminated from the list if even one phase fails the compositional tolerance. The newly created tie simplex $\Delta_{\mathrm{t}}^{\mathcal{R}_{\mathrm{i}}}$, together with the list of tie simplices that are within tolerance $\{\Delta^{\mathcal{R}_{\mathrm{i}}}\}_{\gamma}$, are passed to the discretisation routine.

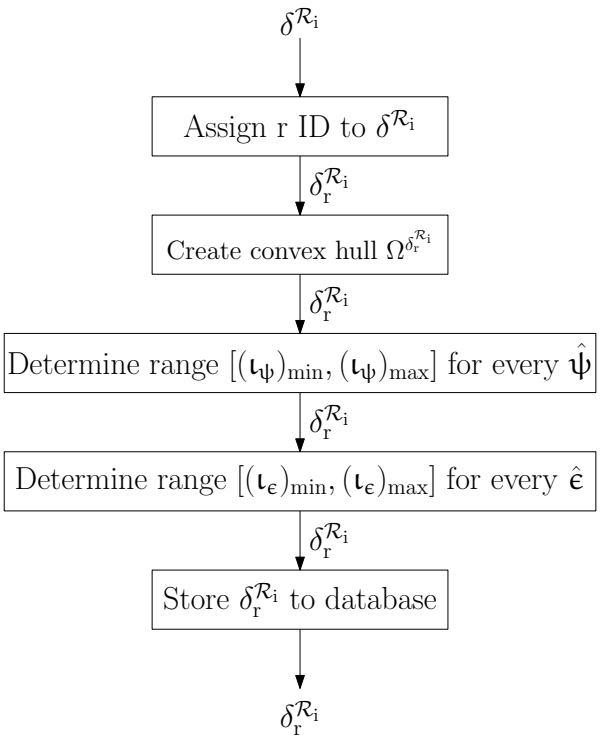

Figure 15: Phase region cell storage routine flow diagram.

Storing Phase Region Cells. Figure 15 shows the flow diagram of the phase region cell storage routine. When a phase region cell is created, a unique ID, r, is assigned to it $\delta_{\mathrm{r}}^{\mathcal{R}_{\mathrm{i}}}$. The temperature and composition of each phase of each tie simplex that the phase region cell is composed of, are used to create a convex hull of the phase region cell, $\Omega^{\delta_{\mathrm{r}}^{\mathcal{R}_{\mathrm{i}}}}$. The convex hull [16] creates the smallest convex set of temperature-phase composition coordinates wherein the phase region cell can be found.

The range of reference frame cell indices of each non-compositional potential that the phase region cell is found in $[(\iota_{\psi})_{\min}, (\iota_{\psi})_{\max}]$, as shown in Figure 11c, is determined. The same is done with the each of the chemical potentials' reference frame indices $[(\iota_{\epsilon})_{\min}, (\iota_{\epsilon})_{\max}]$.

The complete description of the phase region cell is; (1) the phase region cell ID r, (2) the convex hull of the phase region cell $\Omega^{\delta_{\mathrm{r}}^{\mathcal{R}_{\mathrm{i}}}}$, (3) the ranges of each non-compositional potential's indices $[(\iota_{\psi})_{\min}, (\iota_{\psi})_{\max}]$, and (4) the ranges of each chemical potential's indices $[(\iota_{\epsilon})_{\min}, (\iota_{\epsilon})_{\max}]$ that contain the phase region cell. The phase region cell, together with its complete description, is stored to the database.

Recalling Phase Region Cells. Figure 16 shows the flow diagram of the phase region cell recall routine. When an equilibrium calculation has to be performed at a specified system state $\mathbf{X}^{\sigma}$, the database is first queried to determine if a phase region cell is available to create an interpolated tie simplex with. The non-compositional $\mathbf{I}^{\Psi}$ and compositional $\mathbf{I}^{\epsilon}$ potential index arrays correspond-

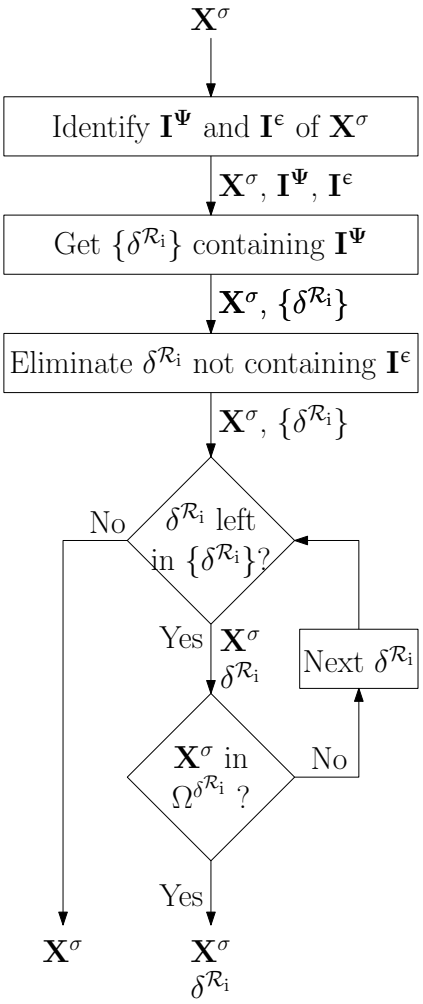

Figure 16: Phase region cell recall routine flow diagram.

ing to the specified state $\mathbf{X}^\sigma$ is first determined. This points to a single reference frame cell.

All phase region cells are stored with the range of each non-compositional potential's indices $[(\iota_\psi)_{\min}, (\iota_\psi)_{\max}]$ and chemical potential's indices $[(\iota_\epsilon)_{\min}, (\iota_\epsilon)_{\max}]$ it spans. All the phase region cells that contain every non-compositional potential index of the system ι_ψ^σ within its stored ranges are recalled and listed $\{\delta^{\mathcal{R}_i}\}$. Each of the recalled phase region cells are then investigated to determine if it contains every chemical potential index of the system ι_ϵ^σ within its stored ranges; if it fails, it is removed from the recalled list $\{\delta^{\mathcal{R}_i}\}$. This is a computationally cheap method of reducing the number of phase region cells that have to be investigated to confirm whether one of them contains the specified state.

The list of identified phase region cells $\{\delta^{\mathcal{R}_i}\}$ are investigated one-by-one to determine whether the system state $\mathbf{X}^\sigma$ is contained within its convex hull $\Omega^{\delta^{\mathcal{R}_i}}$. When a phase region cell is found to contain the specified state, it is passed to the interpolation routine. Otherwise, when no phase region cell is found, the specified system state is passed to the equilibrium calculation software where a direct calculation is performed.

6. Results

6.1. Algorithm Implementation

The algorithm was implemented in Python3 [17]. There are languages that would deliver faster solving times, but for development work it enables fast investigations into different discretisation, storage and recall, and interpolation routines and sub-routines. The thermochemical software used in the algorithm is ChemAppPy [3] - a package that makes the thermochemical data of ChemApp available in Python3. This allowed the algorithm to perform a large number of equilibrium calculations from within Python3.

Python3 also has a large number of powerful compiled libraries that can be used. The Numba library [18] allows for just-in-time compilation of function and classes and improve on the algorithm's performance. SciPy [19] is a powerful library that is used to create convex hulls of phase region cells - even in high dimensions - and efficiently determine if a coordinate is within the convex hull. SciPy is also used to solve the non-linear set of equations to determine the phase compositions of an interpolated tie simplex.

The algorithm will be transferred to another language that provides more performance once the development stage has been completed. The performance of the algorithm, as developed in Python3, is discussed hereafter. The calculations were done in serial on an Intel Core i7-3770 (4 cores) with a clock speed of 3.4 GHz and had 8 GB of RAM available.

6.2. Performance Measurement

The interpolated equilibrium state $\tilde{\mathbf{Y}}^\sigma$ consists of the phase compositions $\tilde{\mathbf{x}}_\epsilon^\varphi$, phase fractions $\tilde{x}_\varphi^\sigma$, and physical $\tilde{\rho}^\sigma$ and thermochemical properties $\tilde{\tau}^\sigma$ of the system. The accelerator is not only developed with a reduction in calculation time in mind but it has to maintain a degree of accuracy as well. Because linear interpolation is employed in the accelerator, some margin of error is expected, and when quantified, can be measured and compared to direct calculation.

Acceleration Factor. The acceleration factor (AF) indicates by what factor the calculation time has been improved by the accelerator with respect to direct calculation, and is shown in Equation (34). When the accelerator's calculation time Δt(accelerator) is less than direct calculation Δt(direct), the acceleration factor is larger than one - calculation time has been accelerated.

$$\mathrm{AF} = \frac{\Delta \mathrm{t(direct)}}{\Delta \mathrm{t(accelerator)}} \tag{34}$$

Phase Composition. To calculate the error being made on the composition of phase i, the distance is determined between the phase's composition as determined by the accelerator $\tilde{\mathbf{x}}_{\epsilon}^{\varphi_i}$ and by direct calculation $\mathbf{x}_{\epsilon}^{\varphi_i}$. The distance is calculated with Equation (35). This provides a positive scalar value that expresses the error being made.

$$\mathrm{d}x_{\epsilon}^{\varphi_i} = \mid \tilde{\mathbf{x}}_{\epsilon}^{\varphi_i} - \mathbf{x}_{\epsilon}^{\varphi_i} \mid \tag{35}$$

Phase Fraction. The difference between the phase fraction of phase i calculated by the accelerator $\tilde{x}_{\varphi_i}^{\sigma}$ and direct calculation $x_{\varphi_i}^{\sigma}$ is determined with Equation (36).

$$\mathrm{d}x_{\varphi_i}^{\sigma} = \tilde{x}_{\varphi_i}^{\sigma} - x_{\varphi_i}^{\sigma} \tag{36}$$

Properties. To measure the accuracy of extensive physical and thermochemical properties, the percentage error between the property calculated by the accelerator and direct calculation, with respect to direct calculation, is determined. The property error calculation for a physical property is shown in Equation (37) and thermochemical property in Equation (38). This is done on the system physical and thermochemical properties only in this evaluation.

$$E\rho^{\sigma}(\%) = \frac{\tilde{\rho}^{\sigma} - \rho^{\sigma}}{\rho^{\sigma}} \times 100 \quad \text{where } \rho \in \{C_p\} \tag{37}$$

$$E\tau^{\sigma}(\%) = \frac{\tilde{\tau}^{\sigma} - \tau^{\sigma}}{\tau^{\sigma}} \times 100 \quad \text{where } \tau \in \{H, S, G\} \tag{38}$$

6.3. Test Conditions

The accelerator algorithm's performance was tested in a number of two- and three-component alloy and slag systems. In each system, 200,000 system states were randomly generated within the entire composition range of each system component and within a temperature range from 500 K up to 50 K above the highest liquidus temperature in the system. A temperature tolerance of 10 K and composition tolerance of 0.001 mol mol^{-1} was specified for all tests.

The performance results are separated based on the number of phases because the algorithm differs between regions with different number of phases. The data shown in the summaries are average values taken over all the equilibrium calculations that were recalled and interpolated.

In single-phase regions, no error is made on the phase composition because linear interpolation is done within a OPF region where the phase composition varies linearly and no error is made on phase fraction as its always one. Because of this, the error made on phase composition and fraction in single-phase regions are omitted from the summaries.

6.4. Two-component Systems

Table 1 shows the results for single-phase regions and Table 2 for two-phase regions in all two-component systems considered.

The acceleration factor for all phase regions in the two-component systems are larger than one - acceleration is achieved. Some systems show more acceleration than others. This is due to the direct calculation time of some systems being longer than others - they show more acceleration. It can be seen that two-phase regions' acceleration factors are higher because when non-compositional potential tie simplices are determined, only one can be created and it automatically becomes the interpolated tie simplex – no additional interpolation steps are required. In single-phase regions, two non-compositional potential tie simplices are created and from there an additional interpolation step is required to determine the interpolated tie simplex.

In two-phase regions, errors made on phase composition are in the order of 1×10^{-5} mol mol^{-1} or less and phase fractions are in the order of 1×10^{-5} or less – very small interpolation errors are made – which is more than satisfactory. The errors made on physical and thermochemical properties are in the order of 1×10^{-2} % or less, which is satisfactory.

6.5. Three-component Systems

Table 3 shows the results for single-phase regions, Table 4 for two-phase regions, and Table 5 for three-phase regions in all three-component systems considered.

The acceleration factor in single and three-phase regions in the three-component systems are larger than one - acceleration is achieved. The two-phase regions require the additional step to find the interpolated tie simplex's phase compositions by solving the non-linear set of equations based on barycentric coordinates. This is an iterative step whose calculation time is longer than direct integration and no acceleration is achieved in these phase regions. This subroutine that solves the non-linear set of equations iteratively needs to be addressed and improved, but at the moment its the only generic solution that could be derived as nothing could be found in literature yet that can be used. It should also be remembered that the direct calculation time in three-component systems are in the order of 0.01 s to 0.001 s and is already fast. In systems with more components and longer direct calculation times, that this accelerator is being developed for, it may be sufficient to use this subroutine requiring further testing, but in this case its not perfect.

It can be seen that three-phase regions' acceleration factors are higher than single-phase regions because when non-compositional potential tie simplices are determined, only one is created and it automatically becomes the interpolated tie simplex – no additional interpolation steps are required. This is always the case in phase regions where $\hat{\varepsilon} - \hat{\zeta}^{\sigma} = \hat{\varphi}$; two-phase regions

Table 1: Summary of algorithm performance in single-phase regions in two-component systems.

System	$\overline{\text{AF}}$ Recalled	$\overline{E\rho^{\sigma}}$ (%)	$\overline{E\tau^{\sigma}}$ (%)		
		C_p	H	S	G
Al−Cu	5.5	8.9e-04	5.8e-02	2.1e-03	4.0e-03
Al−Mn	7.2	6.5e-04	4.9e-02	1.1e-03	2.8e-03
Al−Zn	5.1	1.2e-03	8.0e-04	2.0e-03	1.8e-03
Al_2O_3−CaO	1.8	7.4e-02	5.7e-04	5.0e-04	2.2e-04
Al_2O_3−MgO	5.0	9.9e-02	3.7e-04	6.4e-04	2.4e-04
Al_2O_3−SiO_2	2.6	1.9e-01	2.0e-04	6.6e-04	1.5e-04
CaO−SiO_2	3.1	3.0e-02	8.1e-04	1.2e-03	2.7e-04
Fe−C	2.6	1.5e-03	1.6e-03	1.7e-03	3.5e-03
Fe−Cr	4.1	8.6e-03	6.5e-04	1.3e-03	1.4e-03
Fe−Si	11.1	2.3e-02	9.7e-02	1.1e-03	4.2e-03

Table 2: Summary of algorithm performance in two-phase regions in two-component systems.

System	$\overline{\text{AF}}$ Recalled	$\overline{\mathrm{d}x_{\epsilon}^{\varphi_i}}$	$\overline{\mathrm{d}x_{\varphi_i}^{\sigma}}$	$\overline{E\rho^{\sigma}}$ (%)	$\overline{E\tau^{\sigma}}$ (%)		
				C_p	H	S	G
Al−Cu	11.5	5.0e-07	6.8e-06	2.9e-02	1.5e-03	6.6e-04	5.3e-04
Al−Mn	13.8	7.8e-07	1.6e-05	3.4e-02	5.5e-03	6.6e-04	4.8e-04
Al−Zn	9.9	1.2e-05	1.2e-05	5.9e-02	4.7e-03	6.4e-04	1.2e-03
Al_2O_3−CaO	3.2	4.0e-08	3.0e-07	2.8e-03	5.5e-06	1.9e-04	2.3e-05
Al_2O_3−MgO	8.5	2.6e-07	7.2e-07	4.3e-02	1.4e-05	7.8e-05	8.3e-06
Al_2O_3−SiO_2	6.2	8.7e-07	1.6e-06	6.2e-03	1.5e-05	8.6e-05	9.6e-06
CaO−SiO_2	5.0	9.3e-08	3.4e-07	4.6e-03	6.4e-06	1.6e-04	2.2e-05
Fe−C	4.8	7.6e-08	2.8e-07	1.7e-03	2.3e-03	2.6e-04	8.2e-04
Fe−Cr	10.5	7.2e-06	4.6e-06	3.8e-02	3.7e-03	4.3e-04	1.3e-03
Fe−Si	19.5	1.7e-07	9.2e-07	1.5e-02	1.2e-03	3.5e-04	2.0e-04

Table 3: Summary of algorithm performance in single-phase regions in three-component systems.

System	$\overline{\text{AF}}$ Recalled	$\overline{E\rho^{\sigma}}$ (%)	$\overline{E\tau^{\sigma}}$ (%)		
		C_p	H	S	G
Al−C−Mn	14.2	1.1e-03	3.5e-03	1.1e-03	2.8e-03
Al−Fe−Si	21.1	7.2e-03	2.5e-01	2.5e-03	6.3e-03
Al−Mn−Si	15.2	6.4e-04	1.1e-02	9.9e-04	3.7e-03
CaO−MgO−SiO_2	20.5	1.5e-02	3.8e-03	4.4e-03	1.4e-03
Al_2O_3−CaO−MgO	5.3	5.6e-03	3.8e-04	1.8e-03	7.9e-04
C−Fe−Mn	6.6	3.2e-03	4.0e-03	3.9e-03	7.7e-03

Table 4: Summary of algorithm performance in two-phase regions in three-component systems.

System	$\overline{\text{AF}}$ Recalled	$\overline{\mathrm{d}x_{\epsilon}^{\varphi_i}}$	$\overline{\mathrm{d}x_{\varphi_i}^{\sigma}}$	$\overline{E\rho^{\sigma}}$ (%)	$\overline{E\tau^{\sigma}}$ (%)		
				C_p	H	S	G
Al−C−Mn	0.2	9.4e-04	5.0e-04	5.8e-02	1.3e-01	3.9e-02	4.7e-02
Al−Fe−Si	0.8	9.1e-04	1.2e-03	3.1e-01	7.0e-01	4.2e-02	8.2e-02
Al−Mn−Si	0.4	1.0e-03	1.4e-03	9.3e-02	8.8e-01	6.6e-02	7.2e-02
CaO−MgO−SiO_2	0.2	1.2e-03	1.0e-03	2.2e-01	5.7e-02	2.1e-02	3.9e-02
Al_2O_3−CaO−MgO	0.1	1.1e-03	1.2e-03	1.5e+00	8.9e-02	8.3e-02	8.7e-02
C−Fe−Mn	0.3	1.2e-03	8.7e-04	1.4e-01	2.2e-01	5.9e-02	7.1e-02

Table 5: Summary of algorithm performance in three-phase regions in three-component systems.

System	$\overline{\text{AF}}$ Recalled	$\overline{\mathrm{d}x_{\epsilon}^{\varphi_i}}$	$\overline{\mathrm{d}x_{\varphi_i}^{\sigma}}$	$\overline{E\rho^{\sigma}}$ (%)		$\overline{E\tau^{\sigma}}$ (%)	
				C_p	H	S	G
Al–C–Mn	27.3	3.0e-07	1.7e-06	1.1e-02	2.6e-03	4.4e-04	3.8e-04
Al–Fe–Si	60.8	8.1e-07	1.9e-06	2.0e-02	1.4e-03	4.3e-04	2.0e-04
Al–Mn–Si	46.8	7.5e-07	1.5e-06	5.2e-03	1.6e-03	6.0e-04	3.8e-04
$CaO–MgO–SiO_2$	29.7	3.8e-02	1.8e-02	3.5e-03	1.6e-06	1.8e-05	2.4e-06
$Al_2O_3–CaO–MgO$	14.3	5.0e-02	1.3e-02	2.0e-02	2.3e-06	5.8e-05	6.3e-06
C–Fe–Mn	93.2	2.6e-06	7.0e-06	1.8e-02	2.3e-02	7.3e-04	1.4e-03

in two-component systems, three-phase regions in three-component systems, etc. Some systems show more acceleration than others. This is due to the direct calculation time of some systems being longer than others – they show more acceleration.

In two-phase regions, errors made on phase composition are in the order of $1 \times 10^{-3}\,\mathrm{mol\,mol^{-1}}$ or less and phase fractions are in the order of 1×10^{-3} or less which is satisfactory. In the three-phase regions of the alloy systems, errors made on phase composition are in the order of $1 \times 10^{-6}\,\mathrm{mol\,mol^{-1}}$ and phase fractions are in the order of 1×10^{-6} or less. In the slag systems, errors made on phase composition are in the order of $1 \times 10^{-2}\,\mathrm{mol\,mol^{-1}}$ and phase fractions are in the order of 1×10^{-2} or less. There are more three-phase regions consisting of only pure substances in alloy systems as in slag systems, resulting in no phase composition and fraction errors being made, reducing the average errors.

The errors made on thermochemical properties are in the order of $1 \times 10^{-2}\,\%$ or less, which is satisfactory, apart from 1.5 % average error made with $\bar{C}_p$ in two-phase regions of the $Al_2O_3–CaO–MgO$ system. Discontinuities of varying sizes have been found in some thermochemical properties, as calculated with the equilibrium calculation software, at the liquidus temperatures of system components. Interpolating within phase region cells that contain these liquidus temperatures, and therefore these discontinuities, can result in very large errors if the discontinuities are large – hence the large average error being made.

7. Conclusion

A new accelerator algorithm was developed based on phase diagram geometry to include large number of equilibrium calculations into process and multiphysics models more efficiently. The algorithm uses a system's phase diagram to map the thermochemical system to geometric space by storing calculated physical and thermochemical properties in-situ on the phase region boundaries. Even though the in-situ discretisation method is unstructured, a structured reference frame is used to assign compositional and non-compositional potential indices to tie simplices and phase region cells. This results in more efficient recalls as its a computationally cheap method to filter the tie simplices and phase region cells, reducing the number of each to consider during their respective recall routines. Interpolation and the lever rule is employed to calculate phase compositions, phase fractions, and physical and thermochemical properties from stored values, within reasonable accuracy, at system states where equilibrium calculations have not been performed yet. Linear interpolation in geometric space is less computationally expensive than Gibbs free energy minimisation in the thermochemical space.

The Gibbs phase rule, the generality of simplex geometry, the Cayley-Menger determinant, and the generic lever rule, provides a general basis based on sound principles for discretization and interpolation of OPF regions and boundaries, and for the calculation of phase fractions, phase compositions, and thermochemical properties. There is however still room for improvement, the interpolation algorithm in particular where a set of non-linear equations has to be solved iteratively in one of the interpolation steps. This is the most critical part of the algorithm that has to be addressed to improve on efficiency and performance.

The functionality and performance of the algorithm was tested in 10 two-component and 6 three-component systems. The accelerator achieved a maximum acceleration factor of 93 and many of the other systems tested show acceleration factors of more than 10. Interpolation errors made on phase compositions are in the order of $1 \times 10^{-3}\,\mathrm{mol\,mol^{-1}}$ and less, and phase fractions are in the order of $1 \times 10^{-3}\,\%$ and less. Errors made on physical and thermochemical properties, in most systems, are in the order of $1 \times 10^{-2}\,\%$ and less. The algorithm can be migrated to a language that can provide more acceleration performance, but for now the next step is to test the algorithm's functionality and performance in systems with four and five components.

Acknowledgements

The authors would like to thank Ex Mente Technologies for financial support, as well as Glencore through their funding of the Chair in Pyrometallurgical Modelling at the University of Pretoria.

Nomenclature

Thermochemical System Objects

Identifier	Count	
σ		the system
ε	$\hat{\varepsilon}$	chemical element
ζ^{σ}	$\hat{\zeta}^{\sigma}$	system compositional constraint
ϵ	$\hat{\epsilon}$	independent system component
φ	$\hat{\varphi}$	phase
ζ^{φ}	$\hat{\zeta}^{\varphi}$	phase compositional constraint

Compositional Quantities

Scalar	Array	
n	$\mathbf{n}$	amount (mol)
x	$\mathbf{x}$	amount fraction ($\mathrm{mol\,mol^{-1}}$)
a	$\mathbf{a}$	activity
μ	$\boldsymbol{\mu}$	chemical potential ($\mathrm{J\,mol^{-1}}$)
ι^{ϵ}	$\mathbf{I}^{\epsilon}$	storage reference frame index

Degrees of Freedom

f	of phase region
f′	of phase region with one fixed ψ
f″	of phase region with two fixed ψ
f^{φ}	of phase φ considered in isolation

Non-compositional Potentials

ψ	non-compositional potential identifier
$\hat{\psi}$	number of non-compositional potentials
$\mathbf{\Psi}$	$\begin{bmatrix} T & p & \dots & \psi^{\sigma}_{\hat{\psi}} \end{bmatrix}$ array
$\mathbf{I}^{\mathbf{\Psi}}$	$\begin{bmatrix} \iota_T & \iota_p & \dots & \iota_{\psi^{\sigma}_{\hat{\psi}}} \end{bmatrix}$ storage reference frame index array

T	Temperature (K)
p	Pressure (Pa)

Thermochemical Quantities

τ	thermochemical quantity identifier
$\hat{\tau}$	number of thermochemical quantities
$\mathbf{T}$	$\begin{bmatrix} \bar{V} & \bar{H} & \bar{S} & \bar{G} \end{bmatrix}$ array

$\bar{V}$	molar volume ($\mathrm{m^3\,mol^{-1}}$)
$\bar{H}$	molar enthalpy ($\mathrm{J\,mol^{-1}}$)
$\bar{S}$	molar entropy ($\mathrm{J\,K^{-1}\,mol^{-1}}$)
$\bar{G}$	molar Gibbs energy ($\mathrm{J\,mol^{-1}}$)

Physical Properties

ρ	physical property identifier
$\hat{\rho}$	number of physical properties
$\mathbf{P}$	$\begin{bmatrix} \bar{C}_p & \rho & \mu & \kappa & \dots & \rho_{\hat{\rho}} \end{bmatrix}$ array

$\bar{C}_p$	molar heat capacity, constant pressure ($\mathrm{J\,K^{-1}\,mol^{-1}}$)
ρ	mass density ($\mathrm{kg\,m^{-3}}$)
μ	viscosity (P)
κ	thermal conductivity ($\mathrm{W\,m^{-1}\,K^{-1}}$)

Dimensionality

$\mathbb{D}^{\sigma}_{\mathrm{g}}$	system geometric dimensionality
$\mathbb{D}^{\mathcal{B}}$	OPF boundary dimensional characteristics
$\mathbb{D}^{\mathcal{B}}_{\mathrm{f}}$	OPF boundary functional dimensionality
$\mathbb{D}^{\mathcal{B}}_{\mathrm{g}}$	OPF boundary geometric dimensionality

Storage Reference Frame

$\mathcal{D}$	system's phase diagram
$\delta^{\mathcal{D}}$	reference frame cell of phase diagram

Barycentric Coordinate Interpolation

$\beta^{\Delta}_{\mathrm{i}}$	barycentric coordinate weight within $\tilde{\Delta}^{\mathcal{R}_{\mathrm{i}}}$
$\beta^{\mathcal{B}}_{\mathrm{j}}$	barycentric coordinate weight within $\delta^{\mathcal{B}^{\mathrm{i}}_{\mathrm{j}}}_{\psi}$
$\boldsymbol{\beta}^{\Delta}$	Array of $(\hat{\varphi}-1)$ $\beta^{\Delta}_{\mathrm{i}}$ within $\tilde{\Delta}^{\mathcal{R}_{\mathrm{i}}}$
$\boldsymbol{\beta}^{\mathcal{B}}$	array of $(\hat{\Delta}^{\mathcal{R}}_{\psi}-1)$ $\beta^{\mathcal{B}}_{\mathrm{j}}$ within $\delta^{\mathcal{B}^{\mathrm{i}}_{\mathrm{j}}}_{\psi}$
$\mathbf{w}$	barycentric coordinate weight vector of $\delta^{\mathcal{R}_{\mathrm{i}}}_{\psi}$
$\mathbf{B}$	matrix of $\hat{\varphi}$ of $\tilde{\mathbf{x}}^{\mathcal{B}_{\mathrm{j}}}_{\epsilon_{(\psi)}}$

Thermochemical Data Structures

base notation

$\mathbf{X}$	specified state (sp., independent)
$\mathbf{Y}$ $\tilde{\mathbf{Y}}$	equilibrium state (eq., dependent)

Column 1: directly calculated values

Column 2: interpolated equilibrium values indicated with tilde

Interpolated values in arrays only apply to interpolated data structures. E.g $\tilde{\mathbf{x}}^{\varphi_{\mathrm{i}}}_{\epsilon}$ applies to $\tilde{\mathbf{Y}}^{\varphi_{\mathrm{i}}}$, and $\mathbf{x}^{\varphi_{\mathrm{i}}}_{\epsilon}$ to $\mathbf{Y}^{\varphi_{\mathrm{i}}}$.

system (σ)

$\mathbf{X}^{\sigma}$		$\begin{bmatrix} \mathbf{x}^{\sigma}_{\epsilon} & \mathbf{\Psi}^{\sigma} \end{bmatrix}$
$\mathbf{Y}^{\sigma}$	$\tilde{\mathbf{Y}}^{\sigma}$	$\begin{bmatrix} \tilde{\mathbf{x}}^{\sigma}_{\varphi} & \tilde{\boldsymbol{\mu}}^{\sigma}_{\epsilon} & \tilde{\mathbf{T}}^{\sigma} & \tilde{\mathbf{P}}^{\sigma} & \begin{bmatrix} \tilde{\mathbf{Y}}^{\varphi_1} & \dots & \tilde{\mathbf{Y}}^{\varphi_{\hat{\varphi}}} \end{bmatrix} \end{bmatrix}$

phase i (φ_{i})

$\mathbf{Y}^{\varphi_i}$	$\tilde{\mathbf{Y}}^{\varphi_{\mathrm{i}}}$	$\begin{bmatrix} \tilde{\mathbf{x}}^{\varphi_{\mathrm{i}}}_{\epsilon} & \tilde{\mathbf{T}}^{\varphi_{\mathrm{i}}} & \tilde{\mathbf{P}}^{\varphi_{\mathrm{i}}} \end{bmatrix}$

Geometric Data Structures

simplex ($_{\mathrm{k}}\Delta$)

$\nu(_{\mathrm{k}}\Delta)$	content of simplex

tie simplex ($\Delta^{\mathcal{R}_{\mathrm{i}}}$) in phase region i

t		tie simplex identifier
$\Delta^{\mathcal{R}_{\mathrm{i}}}$	$\tilde{\Delta}^{\mathcal{R}_{\mathrm{i}}}$	$\begin{bmatrix} \mathbf{\Psi}^{\sigma} & \tilde{\boldsymbol{\mu}}^{\sigma}_{\epsilon} & \tilde{\mathbf{x}}^{\mathcal{R}_{\mathrm{i}}}_{\epsilon} & \tilde{\mathbf{T}}^{\mathcal{R}_{\mathrm{i}}} & \tilde{\mathbf{P}}^{\mathcal{R}_{\mathrm{i}}} \end{bmatrix}$
$\hat{\Delta}^{\mathcal{R}_{\mathrm{i}}}$		number of tie simplices
$\mathbf{x}^{\mathcal{R}_{\mathrm{i}}}_{\epsilon}$	$\tilde{\mathbf{x}}^{\mathcal{R}_{\mathrm{i}}}_{\epsilon}$	$\begin{bmatrix} \tilde{\mathbf{x}}^{\varphi_1}_{\epsilon} & \dots & \tilde{\mathbf{x}}^{\varphi_{\hat{\varphi}^{\mathcal{R}_{\mathrm{i}}}}}_{\epsilon} \end{bmatrix}$ composition vertices
$\mathbf{T}^{\mathcal{R}_{\mathrm{i}}}$	$\tilde{\mathbf{T}}^{\mathcal{R}_{\mathrm{i}}}$	$\begin{bmatrix} \tilde{\mathbf{T}}^{\varphi_1} & \dots & \tilde{\mathbf{T}}^{\varphi_{\hat{\varphi}^{\mathcal{R}_{\mathrm{i}}}}} \end{bmatrix}$ thermochemical quantities
$\mathbf{P}^{\mathcal{R}_{\mathrm{i}}}$	$\tilde{\mathbf{P}}^{\mathcal{R}_{\mathrm{i}}}$	$\begin{bmatrix} \tilde{\mathbf{P}}^{\varphi_1} & \dots & \tilde{\mathbf{P}}^{\varphi_{\hat{\varphi}^{\mathcal{R}_{\mathrm{i}}}}} \end{bmatrix}$ physical properties
$\{\Delta^{\mathcal{R}_{\mathrm{i}}}\}_{\gamma}$		set of tolerable tie simplices
$\tilde{\Delta}^{\mathcal{R}_{\mathrm{i}}}_{\psi}$		interpolated iso-ψ tie simplex
$\hat{\Delta}^{\mathcal{R}_{\mathrm{i}}}_{\psi}$		number of interpolated iso-ψ tie simplices
$\Delta^{\mathcal{R}_{\mathrm{i}}}_{\varphi_{\mathrm{j}}}$		phase simplex of phase j in the lever rule

The raw and processed data required to reproduce these findings are available to download from `https://mega.nz/folder/sIcQ0RjL#EQ5LPfRs9b-StwQOcmr9Ug`.

phase region i ($\mathcal{R}_{\mathrm{i}}$)

r	discretisation cell identifier
$\delta^{\mathcal{R}_{\mathrm{i}}}$	$\left[\Delta_1^{\mathcal{R}_{\mathrm{i}}} \quad \dots \quad \Delta_{\mathrm{f}+1}^{\mathcal{R}_{\mathrm{i}}}\right]$ discretisation cell
$\delta_{\psi}^{\mathcal{R}_{\mathrm{i}}}$	$\left[\tilde{\Delta}_1^{\mathcal{R}_{\mathrm{i}}} \quad \dots \quad \tilde{\Delta}_{\mathrm{f}+1-\hat{\psi}}^{\mathcal{R}_{\mathrm{i}}}\right]$ interpolated constant $\boldsymbol{\Psi}^{\sigma}$ cell
$\Omega^{\delta^{\mathcal{R}_{\mathrm{i}}}}$	convex hull of $\delta^{\mathcal{R}_{\mathrm{i}}}$

OPF boundary of region i and phase j ($\mathcal{B}_{\mathrm{j}}^{\mathrm{i}}$)

$\delta^{\mathcal{B}_{\mathrm{j}}^{\mathrm{i}}}$	$\left[\mathbf{Y}_1^{\varphi_{\mathrm{j}}} \quad \dots \quad \mathbf{Y}_{\mathrm{f}+1}^{\varphi_{\mathrm{j}}}\right]$ discretisation segment
$\delta_{\psi}^{\mathcal{B}_{\mathrm{j}}^{\mathrm{i}}}$	$\left[\tilde{\mathbf{Y}}_1^{\varphi_{\mathrm{j}}} \quad \dots \quad \tilde{\mathbf{Y}}_{\mathrm{f}+1-\hat{\psi}}^{\varphi_{\mathrm{j}}}\right]$ interpolated constant $\boldsymbol{\Psi}^{\sigma}$ segment
$\tilde{\mathbf{x}}_{\epsilon_{(\psi)}}^{\mathcal{B}_{\mathrm{j}}^{\mathrm{i}}}$	$\left[(\tilde{\mathbf{x}}_{\epsilon}^{\varphi_{\mathrm{j}}})_1 \quad \dots \quad (\tilde{\mathbf{x}}_{\epsilon}^{\varphi_{\mathrm{j}}})_{\mathrm{f}+1-\hat{\psi}}\right]$ array of $\delta_{\psi}^{\mathcal{B}_{\mathrm{j}}^{\mathrm{i}}}$ phase compositions

Tolerances and Performance Measurement

$\Delta T^{\mathcal{D}}$	Temperature tolerance
$\Delta x_{\epsilon}^{\mathcal{D}}$	Composition tolerance
AF	Acceleration factor
Δt(direct)	Direct calculation elapsed time
Δt(accelerator)	Accelerated calculation elapsed time
$\mathrm{d}x_{\epsilon}^{\varphi_{\mathrm{i}}}$	Phase i composition error
$\mathrm{d}x_{\varphi_{\mathrm{i}}}^{\sigma}$	Phase i fraction error
$E\rho^{\sigma}$	Physical property error
$E\tau^{\sigma}$	Thermochemical property error

References

[1] W.A. Roos and J.H. Zietsman. Accelerating complex chemical equilibrium calculations - a review. *CALPHAD: Computer Coupling of Phase Diagrams and Thermochemistry Awaiting final volume and page numbers*, 2022. doi: 10.1016/j.calphad.2021.102380.

[2] J.H. Zietsman and P.C. Pistorius. Modelling of an ilmenite-smelting dc arc furnace process. *Minerals Engineering*, 19:262–279, 2006. doi: 10.1016/j.mineng.2005.06.016.

[3] Ex Mente Technologies. Chemapppy, 2019. URL `https://www.ex-mente.co.za/chemapppy`. Visited on 2020-06-24.

[4] J.H. Zietsman. Efficient storage and recall of slag thermochemical properties for use in multiphysics model. In R.G. Reddy, P. Chaubal, P.C. Pistorius, and U. Pal, editors, *The 10th International Conference on Molten Slags, Fluxes and Salts*, pages 635–644, Seattle, USA, 2016. The Minerals, Metals and Materials Society. doi: 10.1007/978-3-319-48769-4_68.

[5] A. ten Cate, B.J. Geurts, M. Muskulus, D. Koöster, A. Muntean, J. van Opheusden, A. Peschansky, B. Vreman, and P. Zegeling. Modeling and simulation of phase-transitions in multicomponent aluminum alloy casting. pages 117–139, Enschede, The Netherlands, 2008.

[6] K. Qiu, R. Wang, C. Peng, X. Lu, and N. Wang. Polynomial regression and interpolation of thermodynamic data in al-si-mg-fe system. *CALPHAD: Computer Coupling of Phase Diagrams and Thermochemistry*, 48:175–183, 2015. doi: 10.1016/j.calphad.2015.01.005. URL `http://dx.doi.org/10.1016/j.calphad.2015.01.005`.

[7] G. Zhao, X. Li, D. Xu, J. Guo, H. Fu, Y Du, and Y. He. Numerical computations for temperature, fraction of solid phase and composition couplings in ternary alloy solidification with three different dhermodynamic data-acquisition methods. *CALPHAD: Computer Coupling of Phase Diagrams and Thermochemistry*, 36:155–162, 2012. doi: 10.1016/j.calphad.2011.07.002.

[8] D.V. Voskov and H.A. Tchelepi. Compositional space parametrization for miscible displacement simulation. *Transport in Porous Media*, 75:111–128, 2008. doi: 10.1007/s11242-008-9212-1.

[9] D.V. Voskov and H.A. Tchelepi. Tie-simplex based mathematical framework for thermodynamical elibrium computation of mixtures with an arbitrary number of phases. *Fluid Phase Equilibria*, 283:1–11, 2009. doi: 10.1016/j.fluid.2009.04.018.

[10] S.B. Pope and U. Maas. Simplifying chemical kinetics: Trajectory low-dimensional manifolds in composition space. *Cornell University, Ithaca, New York, United States of America, Mechanical and Aerospace Engineering Report FDA 93-11*, 1993.

[11] B.J.D. Liu and S.B. Pope. The performance of in-situ adaptive tabulation in computations of turbulent flames. *Combustion Theory and Modelling*, 9(4):549–568, 2005. doi: 10.1080/13647830500307436.

[12] L. Lu and S.B. Pope. An improved algorithm for in-situ adaptive tabulation. *Journal of Computational Physics*, 228(2):361 – 386, 2009. doi: 10.1016/j.jcp.2008.09.015.

[13] W.D. Callister and D.G. Rethwisch. *Materials Science and Engineering*. John Wiley and Sons, 8th edition, 2011. ISBN 978-0-470-50586-1.

[14] K. Hack. I.3 - phase diagrams. In K. Hack, editor, *The SGTE Casebook*, Woodhead Publishing Series in Metals and Surface Engineering, pages 43–72. Woodhead Publishing, second edition edition, 2008. ISBN 978-1-84569-215-5. doi: https://doi.org/10.1533/9781845693954.1.43. URL `https://www.sciencedirect.com/science/article/pii/B9781845692155500024`.

[15] D.M.Y. Sommerville. *An Introduction to the Geometry of N Dimensions*, volume 1, chapter 8, pages 124–126. Methuen and Co. Ltd, 36 Essex Street W.C. London, 1929.

[16] R.T. Rockafellar. *Convex Analysis : (PMS-28).*, chapter 1, pages 3–40. Princeton University Press, 1997. ISBN 9780691015866.

[17] G. Van Rossum and F.L. Drake. *Python 3 Reference Manual*. CreateSpace, Scotts Valley, CA, 2009. ISBN 1441412697.

[18] S.K. Lam, A. Pitrou, and S. Seibert. Numba: A llvm-based python jit compiler. In *Proceedings of the Second Workshop on the LLVM Compiler Infrastructure in HPC*, pages 1–6, 2015.

[19] P. Virtanen, R. Gommers, T.E. Oliphant, M. Haberland, T. Reddy, D. Cournapeau, E. Burovski, P. Peterson, W. Weckesser, J. Bright, S.J. van der Walt, M. Brett, J. Wilson, K.J. Millman, N. Mayorov, A.R.J. Nelson, E. Jones, R. Kern, E. Larson, C.J. Carey, İ Polat, Y. Feng, E.W. Moore, J. VanderPlas, D. Laxalde, J. Perktold, R. Cimrman, I. Henriksen, E.A. Quintero, C.R. Harris, A.M. Archibald, A.H. Ribeiro, F. Pedregosa, P. van Mulbregt, and SciPy 1.0 Contributors. SciPy 1.0: Fundamental Algorithms for Scientific Computing in Python. *Nature Methods*, 17:261–272, 2020. doi: 10.1038/s41592-019-0686-2.